Surging of a Hudson Strait Scale Ice Stream: Subglacial hydrology matters but the process details don't

Matthew Drew[1] and Lev Tarasov[1]

[1]Department of Physics & Physical Oceanography, Memorial University of Newfoundland, St John's, Canada

Correspondence: Matthew Drew (mdrew@mun.ca)

Abstract. While subglacial hydrology is known to play a role in glacial dynamics on sub-annual to decadal scales, it remains unclear whether subglacial hydrology plays a critical role in ice sheet evolution on centennial or longer time-scales. Furthermore, several drainage topologies have been inferred but it is unclear which drainage topology is most applicable at the continental/glacial scale. More fundamentally, it is even unclear if the structural choice of subglacial hydrology truly matters for this context.

Here we compare three subglacial hydrology topologies as to their contribution to surge behaviour for an idealized Hudson Strait like ice stream. We use the newly updated model BraHms2.0 and provide model verification tests. BraHms2.0 incorporates each of these systems: two process-based forms dominant in the literature (linked-cavity and poro-elastic) and a non-mass conserving zero-dimensional form (herein termed leaky-bucket) coupled to an ice sheet systems model (the **G**lacial **S**ystems **M**odel ,GSM).

We also assess the likely bounds on poorly constrained subglacial hydrology parameters and adopt an ensemble approach to study their impact and interactions within those bounds.

We find that subglacial hydrology is an important system inductance for realistic ice stream surging but that the three formulations all exhibit similar surge behaviour. Even a detail as fundamental as mass conserving transport of subglacial water is not necessary for simulating a full range of surge frequency and amplitude. However, one difference is apparent: the combined positive and negative feedbacks of the linked-cavity system yields longer duration surges and a broader range of effective pressures than its poro-elastic and leaky-bucket counterparts.

1 Introduction

The role of subglacial hydrology at time scales longer than multiple decades is unclear. Changes in basal coupling due to melt water generation and drainage can occur quickly, leading changes in ice topography and driving stress – even generating changes in flow absent changes in driving stress (*e.g.* subglacial lake drainage events coincident with velocity increases at Byrd and Whillans glacier summarized by Fricker et al. (2016)). Previous studies have inferred subglacial hydrology to play a strong role in internally (*e.g.* Siegfried et al., 2016) and externally (*e.g.* Joughin et al., 1996) driven ice sheet variability on sub-annual to multi-decadal time scales (Retzlaff and Bentley, 1993; Alley et al., 1994; Ou, 2021; Bennett, 2003). Observations beyond these time scales do not exist.

Several subglacial hydrologic systems have been conceptualized (Flowers, 2015). Constraint of the role of hydrological systems is further challenged by the large parametric uncertainties that abound for all choices of drainage topology. For example, the bounds of hydraulic conductivity vary over several orders of magnitude and according to system topology (Werder et al., 2013). These uncertainties hinder widespread adoption of subglacial hydrology models in glacial cycle scale ice sheet modelling (Flowers, 2018). As such, what is needed to adequately incorporate the subglacial hydrologic system into glacial cycle simulations is not understood.

We ask a basic question: does subglacial hydrology matter on longer than decadal time-scales? And if so, to what extent are the structural details of the hydrological system important for this context, especially given the rest of the system uncertainties? Taking a modelling approach, we focus these broad questions to the following: Is basal hydrology needed to capture Hudson Strait scale ice stream cyclicity? If so, should effective pressure be dynamically determined – based on fully mass conserving lateral drainage? Or does a zero-dimensional melt water volume balance with a diagnostic pressure closure suffice? Turning to the parametric uncertainties, which are most important?

Previous model-based tests of Hudson Strait ice stream surging (*e.g.* Calov et al., 2010; Payne et al., 2000; Payne and Dongelmans, 1997; MacAyeal, 1993) have focused on thermomechanical feedbacks but omitted the contribution from the subglacial hydrological system. While these studies capture surges in their simulations based on these limited feedbacks, all models except one (model (d), Calov et al., 2010) implemented an abrupt transition at the frozen-temperate thermal boundary, initiating large scale sliding instantly. This thermal transition is physically unrealistic at the scales of ice sheet modelling, areas larger than 100 km^2 do not become instantly warm based and begin rapidly slide. Instead, the streaming portions of ice sheets transition to faster sliding velocities as their coupling to the bed (effective pressure) decreases. Subglacial hydrology is a potentially important piece of the binge-purge conceptual model of internal oscillations (MacAyeal, 1993) as heat generation from sliding and straining generates melt water.

Here we examine the contribution to ice sheet internal oscillations from the three most dominant forms of distributed subglacial hydrology – linked cavity, poro-elastic, and non-mass transporting leaky-bucket – relative to each other and to no hydrology at all. In the no hydrology case, the transition from frozen to temperate is smoothed to more realistically capture the transition to sliding (as in model (d) of Calov et al. (2010)) following the work of Hank et al. (in prep.). This smoothed temperature transition is also implemented in the subglacial hydrology cases for consistency. We couple these processes to an ice sheet systems model, the **G**lacial **S**ystems **M**odel (GSM).

Simple configurations make system behaviours more interpretable (*e.g.* Calov et al., 2010; Payne et al., 2000). With a realistic bed and actual climate, spatio-temporal variations in model solutions are largely due to the variation in boundary conditions. We therefore model these coupled systems for a simplified North American analogue setup which implements a square bed and flat topography with soft beds in the southern latitudes and in the Hudson Strait/Bay area. The ice sheet is forced with a steady climate and first order feedbacks: Northward cooling temperature trend, vertical lapse rate, and thermodynamic moisture control. The numerical model retains important processes while still being feasible to run large ensembles over a glacial cycle on continental scales to probe parametric uncertainties.

60   Below, we first test the basal hydrology model. This includes demonstration of mass conservation, convergence, and symmetry of BraHms2.0 and verification of its solutions against another prominent model, GlaDS (Werder et al., 2013). Next we show the sensitivity of ice sheet geometry to subglacial hydrologic parameters in comparison with climate and ice sheet parameters. Finally, we present results from a set of 3 large ensembles which compare using no hydrology, linked-cavity, poro-elastic, and leaky-bucket hydrology by contribution to HS surge events.

2   Subglacial Hydrology

In the context of continental scale ice sheet modelling, resolving individual drainage elements and multiple topologies present within the domain is not computationally feasible. In this section we briefly overview some structural choices made by others and present the options compared in this study, beginning with the current understanding of subglacial hydrology and progressing to increasingly approximate representations of it.

70   Water in the subglacial system flows either through inefficient drainage systems (pressure $\propto$ flux) and efficient drainage systems (pressure $\propto$ flux^{-1}) (Flowers, 2015). Inefficient distributed networks are widespread under temperate areas of ice sheets, whereas efficient channel networks are discrete, localized elements. Each class evolves to the other and the change is controlled by system throughput, *i.e.*, water flux. Any mass transporting hydrology model should have three main components:mass conservation describing transport, flow law describing flux as a function of hydraulic gradient and basal water thickness, and a

75   pressure closure.

2.1   Inefficient flow

In the inefficient drainage regime, flux and water pressure rise together. Several inefficient drainage systems have been theorized: thin film, porous media, and linked-cavities. Of these, poro-elastic and linked-cavity (*e.g.* Flowers, 2000; Walder, 1986) dominate recently published models (de Fleurian et al., 2018) and as such these are the two systems we model and contrast

80   herein.

In the poro-elastic formulation, water can drain through the pore space of some permeable surficial material (*e.g.* till). Increasing subglacial water pressures expand the pore-space and modify the permeability of the porous medium to flowing water. The conceptual basis for this system is examined in greater detail by Flowers and Clarke (2002). The pressure closure has no theoretical basis and is based on a power law with empirically constrained parameters.

85   In the linked-cavity system, cavities within the base of the ice open up as basal ice flows over and around bed protrusions – fast flow and larger objects beget larger cavities (Kamb, 1987). As cavities grow larger and numerous they form a connected network linked through smaller orifices giving a tortuous drainage network.

The substrate type that controls which inefficient system dominates – *i.e.*, till cover and roughness – is variable (Pelletier et al., 2016; Brubaker et al., 2013). Conceivably, while poro-elastic drainage requires a porous ice sheet substrate, the cavities

90   can form in any environment with bed protrusions which are less mobile than ice flow. A soft bedded cavity has been seen at the base of a borehole in ice stream C (Carsey et al., 2002) and the theoretical basis for these cavities (Schoof, 2007) is

motivated by drumlin formation (Fowler, 2009). However, cavities can only drain water once they grow enough to join and form a connected network.

The contrast in the larger, order km more model scale and smaller, order metre process scale permits inefficient flow to be

95 described as a continuum at the macro scale. On the macro scale, flux is related to water thickness and hydraulic gradient as (Flowers, 2015):

$$\boldsymbol{Q} = -k h_{wb}{}^{\alpha} |\boldsymbol{\psi}|^{\beta-2} \boldsymbol{\psi} \tag{1}$$

with flux $\boldsymbol{Q}$, hydraulic conductivity k, and subglacial (basal) water thickness h_{wb}. The gradient of the hydraulic potential is given by

100 $$\boldsymbol{\psi} = \boldsymbol{\nabla} \left[P_{water} + \rho_w g z_b \right] \tag{2}$$

with subglacial water pressure P_{water}, density of freshwater ρ_w, gravitational acceleration g, and basal topographic elevation z_b. The exponents in eqn. 1 set laminar or turbulent flow. $\alpha = 1$ and $\beta = 2$ gives Darcy's law for laminar flow through porous media (Darcy, 1856; Muskat, 1934). $\alpha = 5/4$ and $\beta = 3/2$ gives the Darcy-Weisbach relation for turbulent flow through conduits (Clarke, 1996; Weisbach, 1855). Eqn. 2 and 1 are combined with a water pressure closure relationship given by the

105 underlying physical system to get the formulations in § 2.1.1 and 2.1.2.

2.1.1 Poro-Elastic System

Pressurized subglacial water flows through the pore-space of a layer between ice and bedrock, conceptualized as the interstitial space between till grains. As water pressure increases, permeability of the porous medium rises. Water pressure is related to subglacial water thickness by a non-linear function using pore-space saturation (5). This poro-elastic drainage formulation

110 is laid out in Flowers (2000). The flow law is Darcy's law describing laminar flux as a function of hydraulic gradient and subglacial water thickness. The pressure closure is an empirical relationship between the water column height in the elastic pore-space and subglacial water pressure.

Water transport is given in eqn. 3

$$\frac{\partial h_{wb}}{\partial t} + \boldsymbol{\nabla} \cdot \boldsymbol{Q} = m \tag{3}$$

115 Water sheet thickness, h_{wb}, is a continuum property used to describe the average amount of water in a grid cell, $\boldsymbol{Q}$ is the subglacial water flux and m is the aggregate of sources and sinks. The Darcy flow law is given in eqn 4. This is eqn. 1 with $\alpha = 1, \beta = 2$

$$\boldsymbol{Q} = -K h_{wb} \boldsymbol{\psi}. \tag{4}$$

Water pressure in the elastic pore-space is set by eqn. 5

120 $$P_{water} = P_{ice} \left(\frac{h_{wb}}{h_c} \right)^{7/2} \tag{5}$$

where P_{water} is the subglacial water pressure, similarly P_{ice} is pressure due to weight of overbearing ice, and h_c is the water thickness scalar interpreted as thickness of the pore-space accommodating water.

2.1.2 Linked-Cavity System

As ice flows over protrusions in the bed, cavities open in the lee side. The faster ice flows and the higher the protrusion,
125 the greater the opening rate. The weight of the overbearing ice acts to close the void through viscous creep. The trade off
between these two rates determines the net cavity size change rate. These cavities link through smaller connections and form
a drainage network whose throughput is controlled by orifice size and system tortuosity. As water flows more quickly in the
drainage network, wall melting due to frictional heating at the ice/water interface further opens cavities and the interconnecting
orifices, forming a more efficient system. The flow law is the Darcy-Weisbach relationship for turbulent flux dependent on
130 hydraulic gradient and subglacial water thickness. The pressure closure is based on cavity opening and closing velocities and
mass balance. The Darcy-Weisbach flow law is :

$$\boldsymbol{Q} = -K h_{wb}^{5/4} |\boldsymbol{\psi}|^{-1/2} \boldsymbol{\psi} \qquad (6)$$

This is eqn. 1 with $\alpha = 5/4$ and $\beta = 3/2$ with the hydraulic gradient, $\boldsymbol{\psi}$, in eqn. 2 with $P_{water} = P_{ice} - N_{eff}$. k in eqn. 6 aggregates quantities such as tortuosity, hydraulic gradient across the orifice, cavity density, etc. Completing the set of equations,
135 the pressure closure, N_{eff}, is given by the opening/closing relationship for cavity cross-sectional area with respect to time in
eqn. 7. This has three parts:

- wall melting term ($\propto \boldsymbol{Q} \cdot \boldsymbol{\psi}|$)

- opening from sliding over bed protrusions ($\propto u_b h_r$)

- closing due to overburden pressure (creep) ($\propto N_{eff}^n S$)

140 $$\frac{\partial S}{\partial t} = c_1 \boldsymbol{Q} \cdot \boldsymbol{\psi} + u_b h_r - c_2 N_{eff}^n S \qquad (7)$$

where S is the cavity size, c_1 and c_2 are constants, $\boldsymbol{Q}$ is flux, u_b is basal sliding velocity, h_r is bed protrusion height, $N_{eff} = P_{ice} - P_{water}$, and n is a coefficient from Glen's flow law (Schoof, 2010; Werder et al., 2013). These three actions act to
increase/decrease cavity area.

2.2 Efficient flow

145 In the efficient drainage regime, flux and water pressure are inversely related. Flux in the efficient system occurs in subglacial
tunnels incised into overbearing ice (**?**), down into subglacial sediments (Walder and Fowler, 1994), or hard bedrock (Alley,
1989). Channels eroded into bedrock remain in the same place through time while those formed into ice or sediment can open,
move and close depending on overbearing ice and hydrologic conditions. The most commonly modelled efficient system is the
Röthlisberger channel (R-channel) carved up into the overbearing ice (de Fleurian et al., 2018). Dendritic subglacial tunnels
150 open up into the ice from the base by wall melting due to frictional heat from the contact between ice and flowing water
(Röthlisberger, 1972) – the faster the water, the larger the channel. Counter to the inefficient regime, water pressure and flux
are inversely proportional (Schoof, 2010; Flowers, 2015). As water percolating through the inefficient system flows quickly

Name	Description	Range	Relevant Topology
Kcond	Hydraulic conductivity of cavity network	1.00e-06 1.00e+01	LC
zbRoughTunCrit	Vertical basal roughness height	1.00e-02 2.00e+01	LC, Tunnel
lrRatio	Ratio roughness height to wavelength	1. 20.	LC
Qscale	Tunnel switch criterion scaler	1.00e-03 1.00e+00	Tunnel
rNeffFact	N_{eff} normalization in sliding	1.0e4 1.0e6	LC, PE, LB
Tfroz	Complete freeze point, hydrology system	-1.00e-00 0.00e+00	LC, PE, LB
Kmax	Max hydraulic conductivity	1.00e-06 1.00e+01	PE
kratio	ratio max:min hydraulic conductivity	1.00e+00 1.00e+02	PE
hcrit	h_{wb} quotient in basal water pressure	1.00e-01 5.00e+01	PE, LB
Dr	Drainage rate	1.00e-03 1.00e-02	LB

Table 1. Table of parameter names, descriptions, their numerical ranges, and the subglacial hydrologic system they parameterize used in the ensembles for this study.

enough to give significant wall melting, the system becomes unstable and quickly transitions to a channelized system (Schoof, 2010). Schoof (2010) showed that eqn. 7 bifurcates into the inefficient linked-cavity system and the efficient R-channel system, the switch between the two controlled by flux in the subglacial system. At high fluxes, frictional melting of the tunnel ice wall from fast flowing water becomes a run away effect opening a R-channel into the ice. Canals likely open due to high flux as well in the subglacial system, where energetic water mobilizes sediment along its path (Alley, 1992; Walder and Fowler, 1994).

The conceptual basis for the efficient flow model herein is the R-channel which evolves out of the inefficient system based on high fluxes.

3 Model Description

In this section we describe the models used in this study.

3.1 Subglacial Hydrology Model

The subglacial hydrology model – BraHms2.0 – is an extensive update to v1.0 (Kavanagh and Tarasov, 2018), which involves the addition of linked-cavity and leaky bucket systems, an updated generalized grid, modified convergence criteria, modified flux limiter, and code restructuring. This model uses a finite volume discretization with a staggered Arkawa C grid (fluxes at interfaces). In the case of the 2D mass transporting hydrology setups (poro-elastic and linked cavity), we implement the generalized flux calculation in eqn. 1 with a choice of either the pressure-determining closure of Flowers (2000) or a modified version of Schoof (2010) as in that of Werder et al. (2013) and Bueler and van Pelt (2015). Schoof (2010) shows that the wall melting term in eqn. 7 is unimportant until a critical value is reached and the run away effect opens tunnels (see assumption 1

170 below). As such, the wall melting term is assumed zero until tunnelling is triggered.

$$\frac{\partial S}{\partial t} = u_b h_r - c_2 N_{eff}^n S \tag{8}$$

In this model the cavities are described as a continuum: height of a cavity averaged over protrusion spacing (l_r) is given as $h_{cav} = \frac{S}{l_r}$,

$$\frac{\partial (h_{cav} \cdot l_r)}{\partial t} = u_b h_r - c_2 N_{eff}^n h \cdot l_r.$$

175 The opening term is modified to drop as average cavity thickness rises over the bed protrusion $u_b (h_r - h_{cav})$ as in (e.g.) Werder et al. (2013), and cavities are assumed filled by subglacial water ($h_{cav} = h_{wb}$, see assumption 3). This gives water pressure evolution:

$$\frac{\partial P_w}{\partial t} = \frac{\rho_w g}{\phi_{eng}} \left\{ -\nabla \cdot \mathbf{Q} + m_t - u_b (h_r - h_{wb})/l_r + c_2 [P_{ice} - P_w]^n \right\}. \tag{9}$$

Eqn. 9 is derived in apdx. D1 following Bueler (2014) and is similar to that used in Werder et al. (2013); Hewitt (2013); Bueler
180 and van Pelt (2015).

In order to assess the importance of transport vs pressure determination in surging we implement a non-mass conserving zero[th] order "leaky bucket" scheme: a constant drainage rate counters the melt rate to give basal water thickness in that cell following Gandy et al. (eqn. 3 2019):

$$\frac{\partial h_{wb}}{\partial t} = s_{melt} - s_{drain} \tag{10}$$

185 The leaky-bucket scheme uses the empirical pressure-determining closure of Flowers (2000) shown in eqn 5. with basal water thickness limited between zero and the critical thickness of the pressure closure (h_c in eqn. 5).

Fully modelling the process of efficient drainage of water through the channel system would require very short time steps due to CFL (Courant et al., 1928) restrictions and consequently prohibitively long run times. As such an alternate scheme is used under the assumption that drainage happens far quicker than in the inefficient system (assumption 2). If flux at a cell
190 face exceeds the bifurcation threshold or "critical discharge" of Schoof (2010), water is routed down the background hydraulic gradient (i.e., from topography and ice sheet overburden), filling in potential lows along the way until routed water is depleted or exits the ice sheet. This subglacial melt water routing scheme is a slight modification of the down slope surface melt water routing scheme of Tarasov and Peltier (2006) (i.e., with a modified hydraulic gradient). As subglacial water is routed down hydraulic gradient, minima in hydraulic potential are filled and excess water carried further down gradient until either no water
195 remains or the drainage chain reaches the margin and the remaining water leaves the system. This routing scheme is further discussed in Kavanagh and Tarasov (2018).

3.1.1 Solver

BraHms solves the conservative transport equation for distribution of subglacial water (eqn. 3) and effective pressure evolution equation (eqn. 9) using combined explicit and semi-implicit methods. Time integration is done first with Heun's method for an

200 the initial time step followed by a leap-frog trapezoidal predictor corrector method (Kavanagh and Tarasov, 2018). To avoid time splitting, Heun's method is called after every 10 leap frog steps (varying the number of leap frog steps had little effect on the solution in tests).

3.2 The Glacial Systems Model

The model used here is a fully coupled system of hybrid SIA/SSA ice physics (Pollard and DeConto, 2012) and 3D ice
205 thermodynamics and 1D bed thermodynamics (Tarasov and Peltier, 2007). The climate forcing is background surface temperature trend and elevation dependencies for temperature and precipitation. The basal hydrology model includes a choice of linked-cavity, poro-elastic, or leaky-bucket inefficient drainage along side the efficient drainage tunnel solver. A more detailed description of the GSM is forthcoming Tarasov et al. (in prep.).

3.3 Subglacial Hydrology Model Verification

210 Oreskes et al. (1994) describe model verification in general as the task of demonstrating model veracity, correctly asserting that no model can ever be proven – only disproven. However, this problem is not unique to computational model testing, this is a more philosophical epistemological problem. As Sornette et al. (2007) identifies, we do not prove models, we simply build our trust in them through a series of failed attempts to disprove them. In this section, we document performance on some simple tests which every model should need to pass before any amount of trust is put in it.

215 Following others (*e.g.* Sornette et al. (2007)), we take model verification to be more pedestrian than validation: a test that the computational model actually solves the model equations as intended. Or, as Roache (1997) defines, "solving the equations right." Meanwhile, we take validation as the converse from Roache (1997), "solving the right equations." Validation-wise, in this work we are showing not that the right equations were solved, but that it seems to be of low consequence.

The results presented in this section were done in effort to expose errors in the models, the lowest hanging fruit in gaining
220 confidence in the model solutions. The verification strategy in this section is to satisfy:

1. model solutions are symmetric given symmetric input

2. model solutions converge under increasing spatial and temporal resolution

3. mass is conserved

4. models using similar physics should have similar solutions

225 Using simplified setups, expected behaviours are straightforward and in some cases may be calculated by hand (though hand calculations are not shown here). By using a progression of most simple to increasingly complex model setups for testing, model behaviour can be verified against expected behaviour and shown capable of simulating increasingly realistic environments. Here we demonstrate that the model correctly solves the equations. A progression of forcings and couplings were used – of which the transient, two way coupled solutions from the least stable parameters (while still physical) are shown.

230   Parabolic surface topographies match reasonably well with non-streaming ice sheet topographies (*e.g.* Mathews, 1974). The **S**ubglacial **H**ydrology **M**odel **I**ntercomparison **P**roject (SHMIP) (de Fleurian et al., 2018) uses such an ice sheet surface (depicted in fig. B1) and provides solutions to models using similar physics as the model herein. This therefore provides an ideal test bed. This $SQRT\_TOPO$ surface is given by:

$$z_s = 6.0 \left(\sqrt{x + 5000.} - \sqrt{5000.} \right) + 10. \tag{11}$$

235   and flat base, $z_b = 0$.

    Testing of the linked cavity system with Darcy-Weisbach flux model configuration (eqn. 9 and 6) is shown as this is the most non-linear form and a new addition to the model.

    The basal melt water forcing is a sum of three sinusoids:

$$m_t^{jk} = \frac{melt}{2} \sin \frac{2\pi}{T} t + \frac{melt}{2} + \frac{melt}{4} \sin 12 \frac{2\pi}{T} t + \frac{melt}{4} + \frac{melt}{8} \sin 25 \frac{2\pi}{T} t + \frac{melt}{8} \tag{12}$$

240   with basal sliding (feedback to basal water pressure in 9)

$$u = k_{slide} \frac{\tau_b}{N_{eff}} \tag{13}$$

where $k_{slide} = 5.0 \times 10^1 m/s$ is a scaling constant (effective pressure regularization 10 Pa) and basal shear stress (τ_b) is calculated from the driving stress (τ_d):

$$\tau_b = \tau_d = \rho_{ice} g H \frac{\partial H}{\partial x}. \tag{14}$$

245   Total run duration was 10 kyr and the sinusoidal period (T) was taken to be 10 years for short run time. Melt is given by: basal sliding velocity is calculated dynamically:

3.3.1   Symmetry Test

Spatial symmetry at each spatial resolution was calculated as the sum of the difference between the two ice sheet halves across the divide. This difference is zero for all fields showing perfect symmetry.

250 ### 3.3.2   Temporal Resolution Test

Here we test the effect of changing the length of the time step in the basal hydrology on model solution using the SHMIP $SQRT\_TOPO$ setup (depicted in fig. B1). The per run discrepancy with respect to the shortest time step is seen in fig. 1, calculated as:

$$ERR(\Delta t_i) = \sum_{k}^{N_y} \sum_{j}^{N_x} \left| \Lambda^{jk}(\Delta t_i) - \Lambda^{jk}(\Delta t_{-1}) \right|. \tag{15}$$

255   As a first test of convergence under increasing temporal resolution (decreasing time step length) the hydrology model was run to steady state under SHMIP scenario A (constant 2.5 mm/a). Seeing convergence at shorter time steps for the steady forcing, an unsteady sinusoidal melt water forcing was applied (50 year period, 3.5 mm/yr amplitude). The convergence for the unsteady case is shown in fig. 1 for $\Lambda = N_{eff}$, the effective pressure.
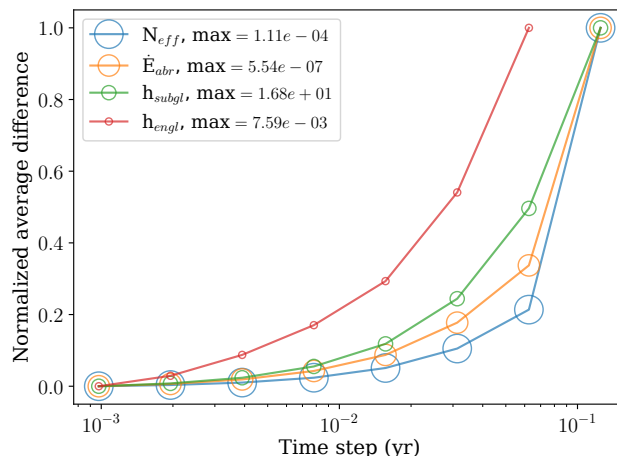
Figure 1. Convergence with decreasing time step. Each field is normalized with the normalization factor shown in the legend (max).

3.3.3 Spatial resolution test

260 Here we show the effect of varying spatial resolution on the model solution. The model was run to steady state with prescribed melt and basal velocity (1.75 m/a ice and 2.0 m/a respectively). For this test the SHMIP setup was used as shown in fig. B1. The $SQRT\_TOPO$ flowline length from divide to toe was set to 100 km and the number of grid cells was adjusted: $\{n_i = 2i + 1\}$ for $i \in [2, 45]$, $i \in \mathbb{N}$ and $\Delta x_i = 100.00$ km$/n_i$, so that the highest resolution was $\Delta x_i = 2.2$ km. The model solution at each resolution was linearly interpolated to the highest resolution grid and the sum of the element-wise difference

265 with the highest resolution used for the error, in keeping with eqn. 15:

$$ERR(\Delta x_i) = \sum_{k}^{N_y} \sum_{j}^{N_x} \left| \Lambda^{jk}(\Delta x_i) - \Lambda^{jk}(\Delta x_{-1}) \right|. \tag{16}$$

Fig. 2 shows the convergence of model solutions (same set as § 3.3.2) at increasing spatial resolution (shorter cell width).

3.3.4 Mass conservation

Mass conservation is demonstrated by comparing flux at the margin to source rates of water or sediment within the ice sheet:

270 the integral of the melt rate over ice sheet less the total flux through the margin will give the basal water thickness change over time. Integrating this change up to each time step will give the basal water thickness at each time step – which can be compared to model calculated basal water thickness in order to assess mass conservation.

To test mass conservation with unsteady input, we applied a sinusoidal melt water forcing (eqn. 12) to the $SQRT\_TOPO$ setup and calculated basal sliding velocity dynamically as in eqn. 13. Here we assume incompressibility of water such that

275 volume is scaled mass.
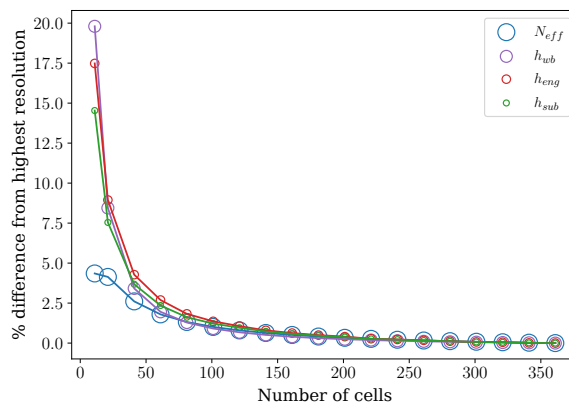
Figure 2. Difference in mean flowline solutions for unsteady SHMIP sqrt ice sheet topography at increasing spatial resolution, at end of 10 kyr run.

A net volume of basal water time series was calculated by time-integrating the net of input and output, $net_{hyd}^{t_i}$, up to each time step t_i:

$$net_{hyd}^{t_i} = \int_0^{t_i} \left(\int_{\mathcal{A}} m_t \, da - \oint_{\mathcal{S}} \mathbf{Q} \cdot \mathbf{n} \, dS \right) d\tau. \tag{17}$$

where $\mathcal{A}$ is the area covered by ice, m_t is the melt at the ice sheet base (eqn. 12), $\mathcal{S}$ is the ice margin (interface beyond which
280   ice thickness is zero), $\mathbf{Q} \cdot \mathbf{n}$ is the flux through the margin, The dynamic model outputs from this test are summarized in fig. B2. This mass conservation test shows a maximum error of 0.052% between the model output and the calculation in eqn. 17 (given in eqn. B1).

3.3.5   Comparison with Werder et al. (2013) results for SHMIP

Results for this model are compared with output of the Glacier Drainage System model (GlaDS, Werder et al. (2013)) employ-
285   ing the same physics: a continuum representation of a linked-cavity system with Darcy-Weisbach flux shown in fig. 3. While their model is similar to this one, there are noteworthy differences. Werder et al. (2013) uses an unstructured mesh and finite element discretization, the channel elements are always active (with water exchanged between the channels at the edges and the distributed system at the subdomains). This is in contrast to BrAHMs in which the channel system switches on in a particular cell given a flux criterion (and uses finite volume discretization and a regular Cartesian grid. We therefore use the SHMIP
290   scenario in which the least amount of channelized flux is active in order to get the most structurally consistent comparison between the two models. BrAHMs closely reproduces the flux and effective pressure solutions for this scenario, concluding our verification that we solved the equations "right."
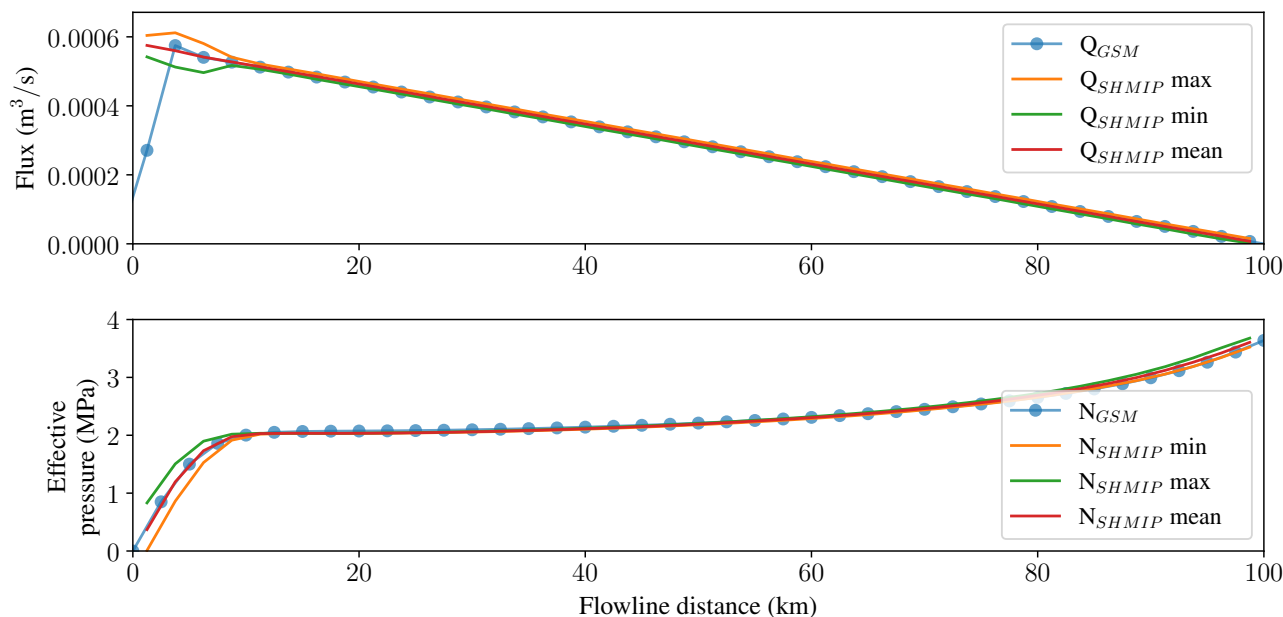
Figure 3. Comparison of our model solution with the SHMIP tuning set which used output from the model of Werder et al. (2013) which uses similar physics to BraHms in the linked-cavity configuration.

4 LISsq Experimental Design

Using a simple setup without externally driven variability from topography, complex land-sea mask, and an unsteady climate,
295 system behaviour is due to the initial transient response and internal feedbacks. Our **L**aurentide **I**ce **S**heet **sq**uare (LISsq) setup includes broad features of the North American bed (fig. 4) and computationally cheap first order diagnostic climate as steady forcing with ice sheet thickness feedbacks. The simple climate allows a free southern margin determined by the background temperature and feedbacks giving a dynamically determined ice sheet geometry. Next we present the design choices of this setup in three categories: bed, climate, and glacial systems.

300 ### 4.1 Bed

LISsq aims to probe the effect of large scale hard to soft bed transitions characteristic of North America. This simplified setup allows separating out the internal feedbacks from the externally forced elements (*e.g.* variability from real topography and land-sea mask and unsteady, spatially varying climate). The shorter run times of this setup also allow larger ensembles, giving a better probe of the parameter space. The simplicity helps with model verification as any variability in the model stems purely
305 from the encoded physical processes.
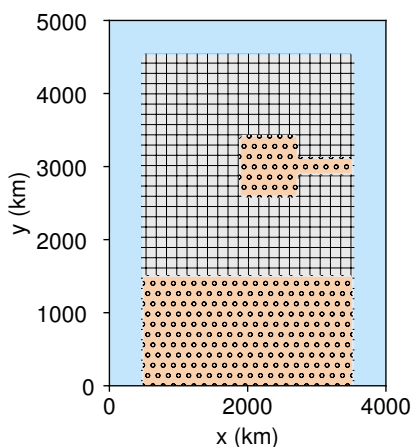
Figure 4. This map of the LISsq bed configuration shows the extent of the domain and the position of the Hudson Bay/Strait and Southern soft beds. Grey hatched regions are hard bedded, beige dotted regions are soft bedded, and blue represents water where ice is ablated.

The majority of the inferred late-Pleistocene Laurentide substrate has been hard bedded (Clark et al., 2006), with unconsolidated sediment cover at the south and in the Hudson Bay/Strait. The HEINO experiments were conducted over similar length scale hard beds with the same soft bedded Hudson bay/strait at the centre of the hard bed. HEINO differed in that it included a circular continental configuration beset on all sides by quickly ablating ocean – the ice sheet geometry was largely set. Here we wish to examine surge behaviour for a variety of ice sheet geometries within the roughly approximate range of the Laurentide length scales and bed. As such, a rectangular bed geometry is set with the boundary of the soft bedded south at a constant latitude and an equilibrium line which is free to evolve with a changing ice sheet.

4.2 Climate

The LISsq climate prescribes a linear background temperature trend with lapse rate feedback. The annually averaged surface temperature, T_{surf} is:

$$T_{surf} = T_{north} + [\![0, T_{grad}y]\!] + LH \tag{18}$$

where T_{north} is the ground level temperature at northern end in °C, T_{grad} is the latitudinal warming rate in °C/km, L is the slope temperature lapse rate (°C/km), and H is ice sheet thickness (m, recall the bed is at constant elevation and glacial isostatic adjustment is not included). The brackets, $[\![\ ]\!]$, denote max.

These temperatures are then used together with a positive degree day scheme (PDD) to simulate net seasonal contribution to accumulation and ablation for an annual average temperature. The positive degree day sum assumes 100 day melt season length with temperatures 10 °C warmer than the annual mean, T_{surf}, and melt coefficient in m/PDD. Ablation is then

$$\dot{b}_{melt} = C_{pdd}[\![0.0, 100(T_{surf} + 10)]\!] \tag{19}$$

Table 2. Table of parameter ranges with kernel density/histogram plots showing initial and sieved parameter distribution

Accumulation incorporates the thermodynamic effect on atmospheric moisture content using the August-Roche-Magnus ap-
325 proximation for the Clausius-Clapeyron relationship (Lawrence, 2005) with parameter ranges adjusted for under saturated air.
Accumulation is zero where $T_{surf} \geq 0°$C.

$$\dot{b}_{accum} = p_{ref}e^{h_{pre}T_{surf}} \tag{20}$$

4.3 Glacial systems

We use a subset of the full featured GSM for this setup. Here we omit glacial isostatic adjustment, surface melt water drainage,
330 sediment transport and production, and ice shelves with grounding-line flux and calving model. This is in order to clearly show
the effect of hydrology feedbacks on ice flow and ice thermomechanics.

4.4 Parameter Range Estimation

In this section we justify chosen parameter ranges based on physical and heuristic arguments and current understanding in the
literature.

335 ### 4.5 Hydraulic Conductivity Parametrization

The range of values appropriate for hydraulic conductivity varies according to whether the drainage system is assumed to be
poro-elastic or linked cavity or whether the flux is assumed laminar (Darcian) or turbulent (Darcy-Weisbach). Hydraulic con-
ductivity is not truly known at the continuum-level macro-scale. Here we use a range based on bounding subglacial hydrologic
flow velocities, typical hydraulic gradients, and subglacial water thicknesses.
340   The velocity of water flow in the subglacial channel end-member imposes an upper bound on the linked-cavity end-member
flow velocity in the bifurcated channel-linked-cavity system (Schoof, 2010). Chandler et al. (2013) used dye tracing experi-
ments at a land terminating West Greenland catchment to measure maximum velocities between moulin injection site and the
margin. Their slowest first arrival time gave 1.00 m/s in the efficient drainage regime.
    Fast ice velocities (*e.g.* ≈1 km/a) give a loose lower bound on water flow speed. Assuming the hydraulic gradient is approx-
345 imately equivalent to that imposed by ice sheet and bed topography (*i.e.*, no contribution from basal water pressure) – around
1000 m/56 km (Chandler et al., 2013) ice sheet surface gradient contribution and 500 m/56 km for bed contribution (Morlighem
et al., 2013) – gives a hydraulic gradient of $\psi \approx 240$ Pa/m. Assuming further ranges of 1 mm to 10 m of basal water thick-
ness, flow speeds between 3×10^{-4} and 1×10^0 m/s, gives a range of linked-cavity hydraulic conductivity (Kcond, table. 1)
between 1×10^{-5} and 1×10^{-1} m$^{5/4}$/Pa$^{1/2}$s. To ensure complete bounding, we probe a wider range of 1×10^{-6} and $1 \times 10^{+1}$
350 m$^{5/4}$/Pa$^{1/2}$s. Flowers (2000) assessed the range of hydraulic conductivities to be Kmax $= 1m/s$ and $k_{min} = 10e-7m/s$. The
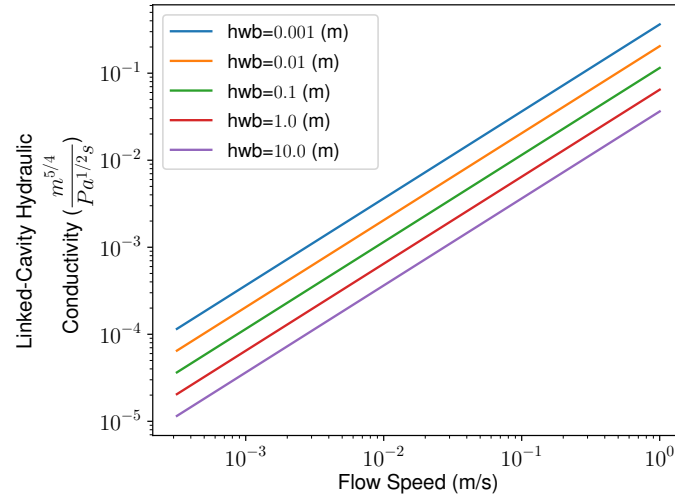
Figure 5. Range of linked-cavity hydraulic conductivities based on velocities, hydraulic gradient, and basal water thickness ranges in the text – using $K = \frac{v}{\psi^{1/2}h^{1/4}}$.

poro-elastic hydraulic conductivity increases as the pore-space fills with melt water as:

$$log(K) = \frac{1}{\pi}\left[log(\text{Kmax}) - log\left(K_{min}\right)\right] arctan\left[k_a\left(\frac{h_{wb}}{\text{hcrit\_dpe}} - k_b\right)\right] + \frac{1}{2}\left[log(\text{Kmax}) + log\left(K_{min}\right)\right] \tag{21}$$

where K is the poro-elastic hydraulic conductivity, Kmax is the maximum conductivity, $K_{min} = \text{Kmax}/\text{kratio}$ is the minimum conductivity, hcrit_dpe is the critical water thickness in the pore-space (h_c in eqn. 5 and in tbl. 1), and k_a and k_b control the transition between the maximum and minimum conductivity.

Hydraulic conductivity in both the poro-elastic and linked cavity formulations is defined at the cell centres and is a function of cell temperature relative to pressure melt point (Tbp). To account for the transition from fully cold based (frozen) to fully warm based (thawed), the bed is assumed to be fully frozen below T_{froz} and the hydraulic conductivity is given the following dependence on Tbp:

$$K^{i,j} = (K_{cond} - K_f) * \left(1 - \exp\left[3\llbracket min\left(0.0, Tbp^{i,j}\right), T_{froz}\rrbracket/T_{froz} - 1\right]\right) + K_f \tag{22}$$

As the flux should be a function of the potential difference across the interface, the harmonic mean of the adjacent cell centred conductivities gives the most appropriate interface conductivity (Patankar, 1980).

$$K_{we}^{ij} = \frac{2K^{i-1j}K^{i,j}}{K^{i-1j} + K^{ij}} \tag{23}$$

4.6 Basal roughness

The height of bedrock protrusions relevant to subglacial cavity formation and its spatial variation lacks assessment in the literature and justified values are difficult to come by. The height of these protrusions, or terrain roughness, affects several

basal processes in glaciated regions, including heat generation in basal ice, sliding, subglacial cavity opening, and bedrock quarrying. Length scales relevant to subglacial cavity formation have been estimated from chemical alteration of bedrock (deposition of calcium carbonate precipitates) (Walder and Hallet, 1979). These cavity outlines form during sliding-associated-

370 regelation when water refreezes at the glacier substrate in the lee side of bedrock highs, precipitating dissolved carbonates. The deposits in this study indicate cavities 0.1-0.15 m high. Several studies then use a value in this range (Werder et al., 2013, *e.g.*). Kingslake and Ng (2013) refers to Walder (1986) for this value, but Walder (1986) does not provide any justification for it in their table 2 and do not refer explicitly to the earlier work of (Walder and Hallet, 1979).

In deglaciated areas with bed access, quantifying roughness at the ice sheet scale is a non-unique problem and measures

375 abound. For example: standard deviation of elevation, power spectral density of elevation, and local bed slope. These are relative measures which do not identify the typical prominence of roughness features in a domain. What is needed for modelling linked-cavities is the average height of bedrock protrusions relevant to the cavity scale (itself uncertain) at given wavelengths. How these heights vary spatially for previously glaciated regions has not been assessed. Identifying this as a gap in the current glaciological literature, we adopt similar scale values and probe a wide range in order to capture ice sheet sensitivity to the

380 scale of cavity-forming-bump-height. As stated above, Werder et al. (2013) and Kingslake and Ng (2013) both use $h_r = 0.1$ with the latter referring to Walder (1986) who gives a range of 0.01 to 0.5 m for the relevant bump height. Iverson (2012) show cavities and quarrying are intrinsically linked. As such, the step size of quarried surfaces may indicate a scale for cavity growth. Anderson et al. (1982) mapped cavities forming along 1 m high steps at the base of Grinnell Glacier in Montana, United States. Following the same reasoning, the size of quarried boulders also gives an estimate of the upper bound for length scales. 20

385 m boulders, though less common, can be found (though communition in transit may mean the original size distribution was larger). As such, we use a range of $h_r \in [0.01, 20.0]$m and a range for the roughness wavelength as a function of roughness, $l_r \in [1.0, 20.0] \times h_r$.

4.7 Hydrology Temperate Transition

This parameter is used to interpolate between a conducting (at 0ºC) and non-conducting (at a lower bound temperature)

390 hydrologic system with a logic similar to the temperature ramp reasoning. Thus, the range is determined by the work of Hank et al. (in prep.) and the lower bound of the interpolation is probed in the range of $[-1.0, 0.0]$.

4.8 Tunnel switching scalar

The flux threshold switch from inefficient to efficient drainage is given by the ratio of cavity opening due to sliding versus wall melting from viscous heating:

$$Q_{crit} = Q_{scale} \frac{u_b h_r / l_r}{c_1(\alpha)\psi} \tag{24}$$

where u_b is the velocity, h_r / l_r the basal roughness, c_1 a scalar, α the Darcy Weisbach water thickness exponent, ψ the hydraulic gradient. Q_{scale} is a scale factor adjusting for subgrid uncertainty. It is possible that at a subgrid scale, local fluctuations in flux may trigger a run-away tunnelling effect.

4.9 Effective Pressure Normalization

400 This is the value used to normalize the effective pressure in the basal sliding velocity calculation and is set based on typical effective pressures. Effective pressures greater than this parameter values should slow sliding and less than should hasten sliding. We set this range to $[10kPa, 1MPa]$ based on the typical effective pressure values seen in fig. 6. The effective pressure and normalization (rNeffFact) is incorporated into the basal sliding velocity as:

$$u_b = c\tau_b^p \frac{\text{rNeffFact}}{N_{eff}} \tag{25}$$

405 ### 4.10 Basal Sliding Parameters

The soft and hard sliding factors were set to wide bounds somewhat outside the recommended range for the GSM (Tarasov et al. in prep.), the power for soft bedded sliding was kept within the typical range. These ranges were $rmu \in [0.01, 4.0]$, $fslid \in [0.0, 5.0]$, and $POWBtill \in [1, 7]$.

4.11 Climate parameters

410 A range of $[5, 10]^o$C/km is used for slope lapse rate on the basis of PMIP2 Greenland model simulations in Erokhina et al. (2017). The range for T_{north} was obtained from PMIP4 ensemble mean distribution of northern ($> 75^o$) latitude temperatures at LGM in Kageyama et al. (2021) shown in fig. 6a. The precipitation parameter ranges in eqn. 20 were adjusted to bound the range of precipitation and temperatures below freezing in Kageyama et al. (2021), as shown in fig. 6b.

4.12 Ensemble Design and Parameter Sensitivity

415 To understand the effect of hydrology, ensembles for different model configurations are compared: Linked-cavity (LC), poro-elastic (PE), Leaky-Bucket (LB), and no hydrology (NH) – 18816, 19992, 15288, and 11760 runs in each ensemble respectively. Each ensemble varied the hydrology, ice sheet, and climate parameters simultaneously in order to capture parameter interactions and the number of runs was scaled with the number of parameters in each setup (15 in LC, 16 in PE, 12 in LB and 9 in NH). The parameter space is sampled with the quasi-random-low-discrepancy Saltelli extension of the Sobol sequence 420 (Saltelli, 2002) as implemented in SALib (Herman and Usher, 2017) with second order terms enabled. Parameters are sampled with a log uniform distribution for parameter values which vary over orders of magnitude. Each run proceeded for 100 kyr with the first 50 kyr taken as spin up (from no ice, initial accumulation given by the background temperature from T_{north} and T_{grad}).

Ice sheet geometries vary widely among runs for all model configurations. Maximum ice thickness ranges from 0 to ~ 425 6000 m while maximum North-South extent ranges from 0 to 4500 km. Here we study surge behaviour at scale similar to the Laurentide ice sheet by sieving the ensembles based on maximum ice sheet thickness and North-South extent. At **L**ast **G**lacial **M**aximum (LGM, 22 ka) the maximum ice thickness was plausibly around 4000 m (Tarasov et al., 2012). We use this estimate with a lower bound of 3000 m for the sieve in the main study and examined additional sieves with bounds $[2500, 3500]$ and

(a)

(b)
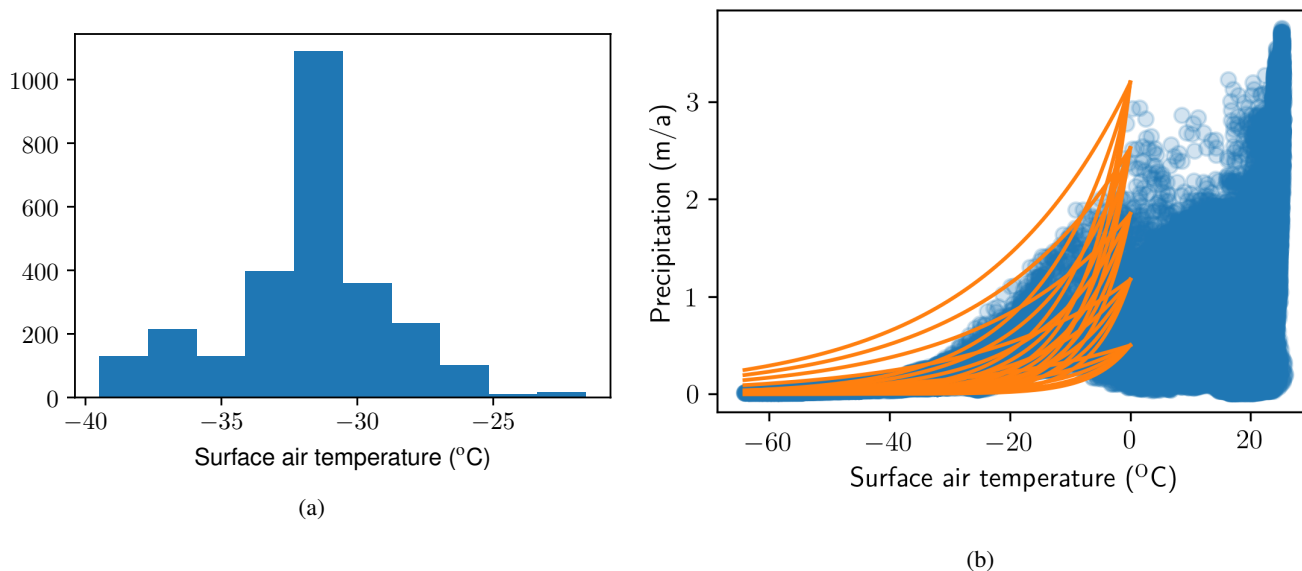
Figure 6. Precipitation and temperature values extracted from PMIP4 (Kageyama et al., 2021) ensemble mean fields at LGM. A histogram of surface air temperatures is shown in a). A scatter plot of precipitation and surface air temperature with overlain precipitation temperature relationships showing the range of parametrizations used is presented in b).

$[3500, 4500]$ in appendices (§ A). LGM North-South extent was $\approx$4000 km, while the last margin to fully encircle the Hudson
430   Bay and Strait (11.50 ka) extended $\approx$2500 km North to South (Dalton et al., 2020).

The importance of hydrology parameters to determining ice sheet geometry can be probed with sensitivity analysis. Local sensitivity analysis methods neglect interaction terms important for studying feedbacks in coupled models and so are not applicable here (Saltelli et al., 2008). Meanwhile variance based (Sobol, 2001) methods require assumptions about the sampling structure of the underlying inputs. The trouble with coupled models is they can be unstable, as such there are incomplete runs
435   which render sampling structure assumptions moot.

We develop a non-parametric method to measure sensitivity: we assess ice sheet geometry sensitivity to parameters by comparing the original uniform input parameter distribution with the parameter distribution corresponding to the sieved geometries (limiting the ensemble to those within geometric bounds). The non-parametric nature alleviates the need to make assumptions about the underlying parametric distribution class (*e.g.* variance is a normal distribution parameter). Using the impact of a sieve
440   on parameter distribution to measure sensitivity means that assumptions about the sampling methodology are not required and that successive sieves can be applied to the ensembles to measure different aspects of model sensitivities. For example, in § 5.1 we measure the sensitivity of surge frequency for those ensemble members which pass the geometry sieve by further sieving on surge frequency. Parameters which are not controlling the ice sheet geometry will have a similar distribution after selecting for that geometry range as the original input sample distribution. The more modified the distribution, the more sensitive the
445   parameter. More precisely, each distribution is approximated with a kernel density function (KDF) normalized to unit area
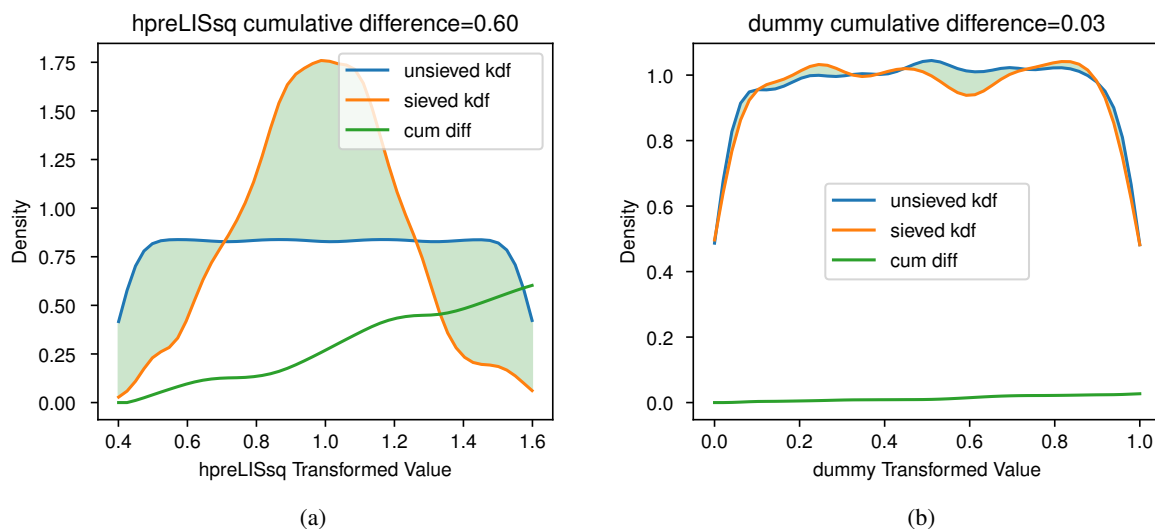
Figure 7. Cumulative kernel density function difference sensitivity metric for the most sensitive parameter, hpre (a) and least sensitive parameter, dummy (b) for the LC setup ice sheet geometry sieve. The parameter values are transformed for input to the GSM. The blue line shows the ensemble total parameter value distribution, orange shows the distribution after sieving the ensemble for geometry, and the green line shows the cumulative (integrated) absolute difference of blue and orange up to that value. The total cumulative difference gives the sensitivity measure, shaded in green.

under the KDF. The sensitivity metric is then the integral of the absolute difference between the sieved and unsieved KDFs, *i.e.*, the measure of how much the sieve modifies each parameter's KDF. For example, the maximum KDF difference would stem from a narrow spike on the sieved distribution, which would mean that parameter strongly controls the model output, *e.g.* the more limited range indicated for hpre in fig. 7a. We add a uniformly sampled dummy parameter not used by the model to

450   set a threshold of accuracy of the sensitivity metric in each case. This dummy parameter has a very similar input and sieved distribution, for example that for the LC geometry sieving in fig. 7b.

     The sensitivity metrics for all parameters in fig. 12 rise above the baseline significance level set by the dummy parameter in each ensemble. The temperature coefficient in the August-Roche-Magnus relation (h_{pre},), North-South temperature gradient and intercept (T_{grad} and T_{north},eqn. 18), and lapse rate are the top four geometry controlling parameters in all cases except

455   LB (though lapse rate is close for this ensemble as well). In the hydrology enabled setups, hydrology parameters rank in the top 5.

     The ranked parameter sensitivity for each model in fig. 12 exhibits an inflection point in parametric sensitivity which we use to determine the number of controlling parameters. This inflection point is an approximate indication of the diminishing sensitivities in the model setup. As such, parameters to the right of this point are taken as sensitive and those to the left are

460   considered insensitive and could be fixed for the purposes of geometry. The change in sensitivity metric from one parameter to the next highest is not strictly monotonic, therefore we fit a third degree polynomial to the metrics and use its coefficients to calculate the inflection point for an estimate of the inflection. Around two-thirds of parameters fall on the right hand side of
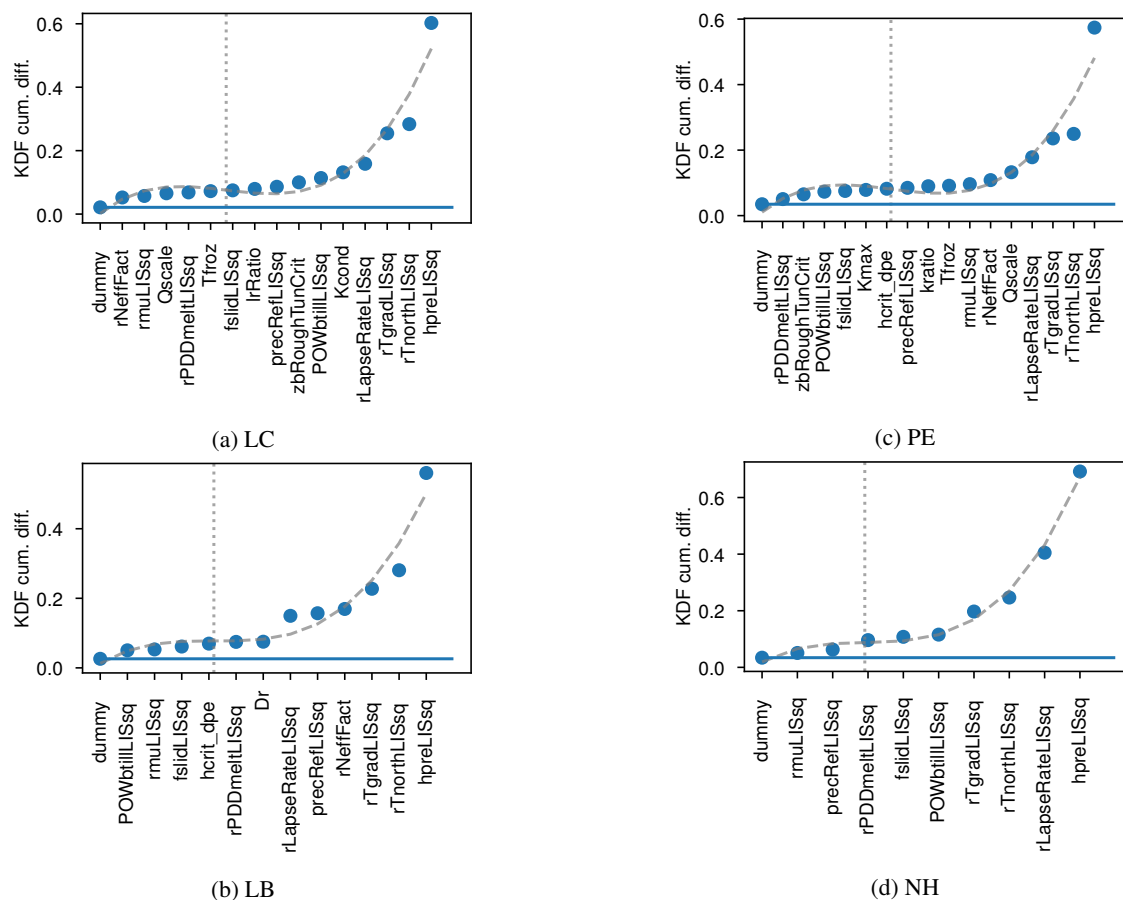
Figure 8. Parameters ranked by relative sensitivity for each model setup: LC (a), LB (b), PE (c), and NH (d). The vertical dotted line indicates the inflection point in the sorted sensitivities used to approximately delineate the transition from insensitive to sensitive parameters. The dotted grey line shows the fitted third order polynomial used to calculate the inflection point.

the inflection in each ensemble. For those hydrology bearing model configurations, half or more of the hydrology parameters lie in the sensitive zone. This shows that subglacial hydrology is even important at the scale of whole ice sheet geometry.

465   The most influential hydrology parameter in the LC setup is hydraulic conductivity which controls the dynamic effective pressure, while in LB and PE the geometry is quite sensitive to the normalization of the effective pressure in basal drag (though PE is more sensitive to the tunnelling tendency, Qscale). In the LC case, the ice sheet geometry is most sensitive to those parameters which control the dynamics of effective pressure themselves (Kcond and zbRoughTunCrit). In the PE case, the parameters controlling the transition to efficient drainage (Qscale) and effective pressure normalization are most important

470 hydrology parameters. These parameters are both diagnostic controls on subglacial water balance and sliding velocity. Similar to PE, the most important subglacial hydrology parameter for LB is the effective pressure normalization.

4.13 Which surge metrics?
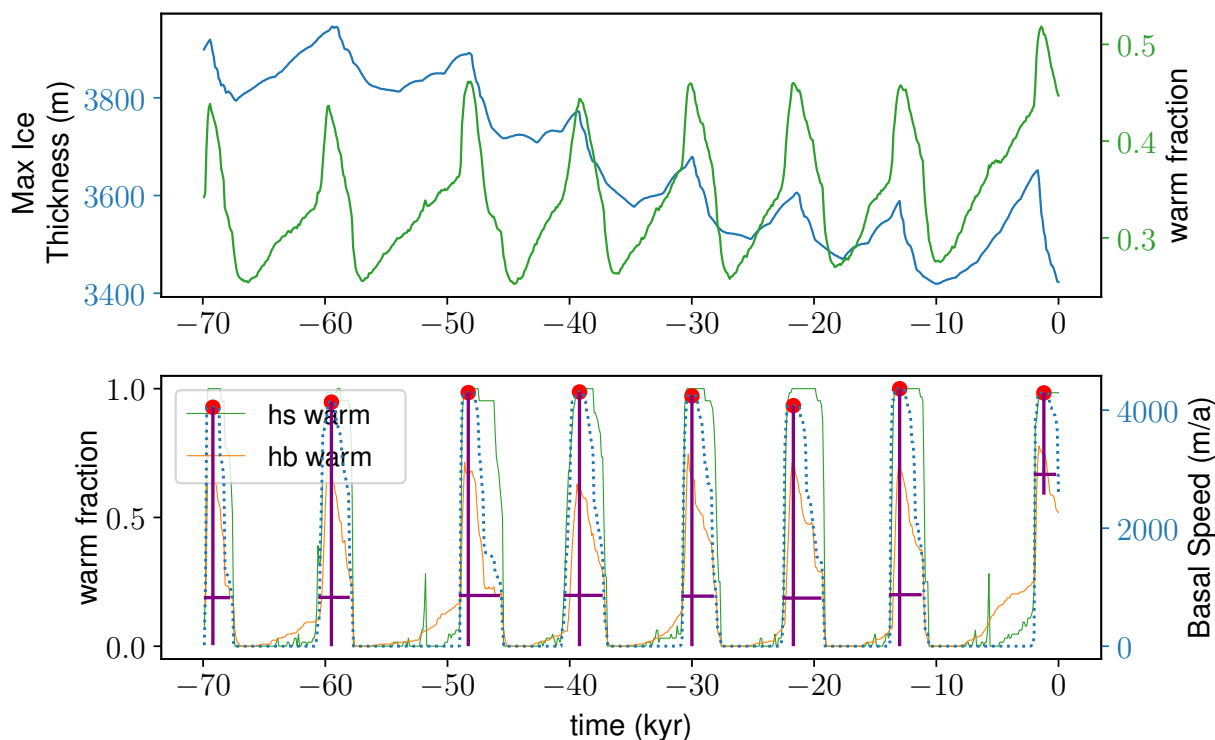
Figure 9. Evolution of the ice sheet and idealized Hudson Strait ice stream showing repeated surge events and how metrics are extracted from a sample run. In the top panel the maximum ice sheet thickness throughout the run is shown with the whole ice sheet area fraction of warm based ice. The bottom panel shows HS basal speed – which is used to pick surge peaks and estimate prominences – along with the area fraction of warm based ice within the HS and its Hudson Bay source region. Red dots show picked event peaks, vertical purple lines give their "strength" (prominence) and horizontal purple lines show their duration.

The two most obvious measures of internal oscillation are amplitude and period. This highly non-linear system does not exhibit sinusoidal behaviour, but we can pick surge metrics which approximate these measures. To this end, each surge type was evaluated in two ways – number of surge events (an indication of periodicity) and strength (or speed increase) of surge events (*i.e.*, amplitude).

The background sliding speed of the actual HSIS in the non-surging state is unknown. While this study does not aim to replicate the actual HS, we are studying the behaviour of an ice stream and sheet with similar dimensions to the HS and Laurentide. As such, labelling and measuring the strength of a surge event needs to be agnostic of quiescent-phase conditions between events. Ice stream acceleration at scales comparable to the HS has not been observed in the modern period. Though significantly smaller than the HSIS and its catchment, the Vavilov ice cap did accelerate from 12 m/a to 75 m/a between 1998 and 2011 CE (Willis et al., 2018). Satellite observations of the North East Greenland Ice Stream (NEGIS) combine with

modelling to show acceleration greater than 1 m/a^2 in places between 1985 to 2018 CE (Grinsted et al., 2022). Therefore we define a surge event in this setup as a large increase in spatially averaged HS basal sliding speed (>1000 m/a, given 25-100

485   year acceleration period) over the background, quiescent-phase speed. Velocity can also change during a surge as portions of ice within the HS accelerate over others. Ice stream shear margins can be regions of the fastest velocity changes and ice stream geometry can change over time (Grinsted et al., 2022). As such, we do not define adjacent short lived changes in velocity as separate surge events.

In order to label surge events, we use peak prominence (Virtanen et al., 2020) – drawn from the concept of topographic

490   prominence (height of local max above adjacent local minima) – to estimate surge events from the basal velocity time series (1 year sample rate) for each run. This allowed surged metrics to be agnostic of any background value. In order to minimize spurious peaks picked on variations in velocity during a single event, a 401 year median filter was applied. This means that abrupt velocity changes lasting ∼200 years or less will not get picked as events. This is less than the lower bound on HSIS surge duration inferred from IRD by Dowdeswell et al. (1995) who estimate that those surges most likely lasted between 250

495   and 1250 yr on the basis of Heinrich Events interpreted in 50 North Atlantic drill cores. A comprehensive review of Heinrich Events and IRD age intervals available in the literature by Hemming (2004) infers a mean duration of 495 years where the lowest estimate is 208 years (tbl. 3). The duration for these modelled surge events is calculated as full width at 80% maximum prominence (height above adjacent local minima).

5   HS Surging

500   Sieving the data by ice sheet geometry cuts the ensemble size to ≈1/3 to 1/4: Poro-elastic (PE) has 3154/19992 (15.7%) runs passing the geometry sieve ($< H_{max} > \in [3000, 4000]$ m and $< \Delta y > \in [2500, 4000]$ km), linked-cavity (LC) 3566/18816 (18.9%), leaky-bucket (LB) 2721/15288 (17.7%), and no hydrology (NH) 1382/11760 (11.8%)runs. The histograms in fig. 10 show the frequency of surge events and strength of speed up of those events in the last 50 kyr of each simulation. The lower bound on of HSIS surge frequency inferred from the Heinrich Event record (Hemming, 2004; Naafs et al., 2013) is 3 in 50

505   kyr. The rate of runs with 2 or more surge events in the sieved results is: 423/3154 (13.4%) for PE, 504/3566 (14.0%) for LC, 836/2721 (30.7%) for LB, and 75/1382 (5.4%) for NH. The distribution of the frequency of surge events stemming from each hydrology setup is not significantly different from the others (though LB does have more surges in the 4-7/50 kyr frequency range), nor is the magnitude of ice stream speed up. The no hydrology case, however does differ from those three: the rate of runs with events is significantly lower and the frequency and strength of events per run are also lower.

510   The duration of HS surge events highlights a difference between the three hydrologies: the trend in duration with increasing numbers of events diverges at a periodicity of 4 events in 50 kyr. In fig. 11a we extract the median surge duration by sieving each ensemble to runs with a given number of events (in addition to the geometry sieve) and compare those trends across the four setups. Frequency levels with ten or fewer runs passing the sieve are omitted as trends degrade around this level of membership.

(a)	(b)
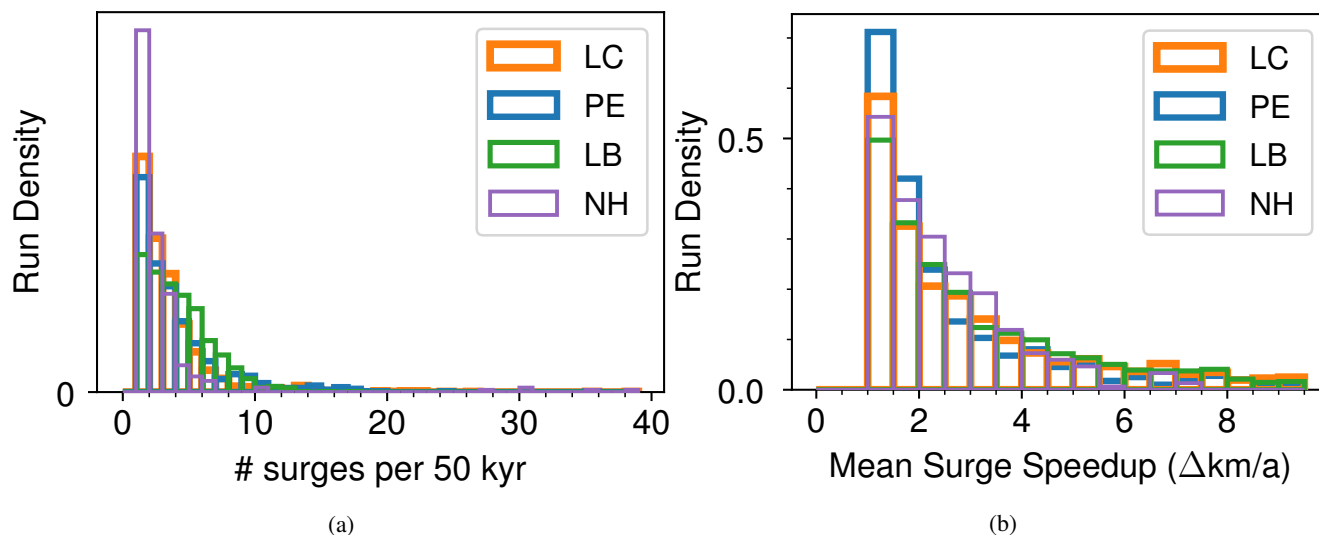
Figure 10. Histograms of Heinrich event metrics per parametrization for each model configuration. The frequency of surge events in a 50 kyr time frame is shown in a). The peak prominence of spatial mean HS velocity over adjacent local minima is shown in b).

As the frequency of surge events in each run increases, the median duration of surges in those runs stays largely flat, perhaps decreasing slightly for both the poro-elastic and leaky-bucket hydrologies. Not so for linked cavity, the duration of surges increases up to the seven surge level where it roughly doubles that of the poro-elastic and leaky-bucket hydrologies. This relationship is stronger still when selecting thinner ice sheets with mean maximum thickness between $[2500, 3500]$ m as shown in fig. A2a. In this geometry range, the surge duration decreases at first, reaching a minimum at 3 surges before steadily increasing in duration until it more than doubles the leaky-bucket surge duration (PE run counts are below the significance threshold). For thicker geometries no differences between the three hydrologies are apparent (fig. A4a).

5.1 Sensitivity of Surge Frequency

Applying a sieve on surge frequency in addition to the geometry sieve highlights the system sensitivity to subglacial hydrology. Fig. 11a shows the sieved result (sieved between three and twelve consistent with the minimum number of Hudson Strait surges inferred from the Heinrich Event record and the maximum number of events in the figure). The sensitivity ranking is insensitive to whether the sieve upper bound is eight or forty events, likely due to the fact that most runs have eight or fewer surge events. For all of the hydrology ensembles, the effective pressure normalization exerts the most control on surge frequency. In the case of the PE and LB ensembles, hydrology parameters give the first and third highest sensitivities – rNeffFact in both cases, Kmax is third for PE and hcrit_dpe is third for LB. For LC, the next hydrology parameters do not appear until seventh and eighth place. This may be due to the dual role rNeffFact plays in the linked-cavity system: it exerts influence on the sliding velocity which in turn controls the cavity opening rate which is proportional to effective pressure. In the NH case, soft bed
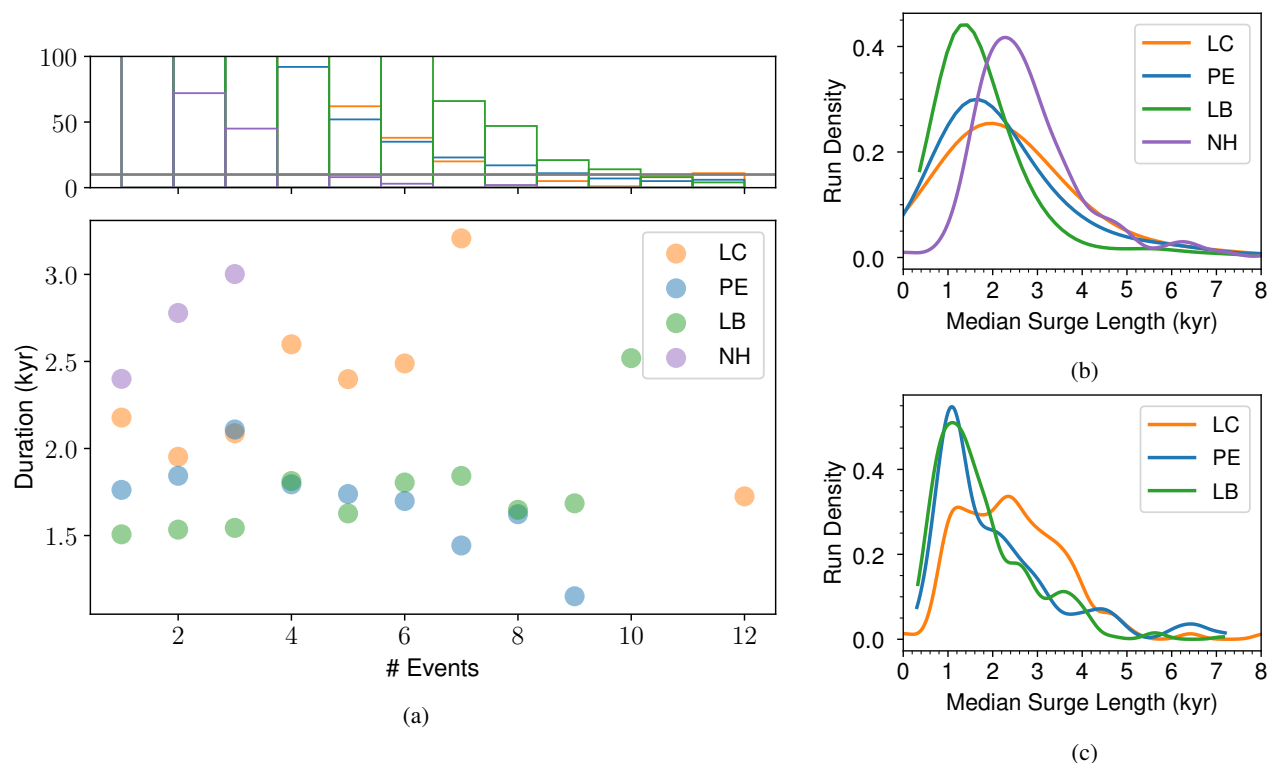
Figure 11. Surge event duration at different frequencies. The scatterplot and histogram in (a) shows trends in median duration with increasing number of surges in a run. The overlying histogram shows the number of runs in each frequency sieve with the 10 run cutoff level shown by the horizontal grey line. The no-hydrology setup falls below this level after the three event bin, and the linked-cavity setup shows a divergence from the other two at this point. (b) and (c) show the kernel density functions of surge duration for runs with one to three and five to seven events respectively.

sliding parameters rmu (soft bed sliding coefficient) and POWbtill (soft bed sliding law power) are the most important for surge frequency. POWbtill is also the second most important parameter in both the LC and PE cases.

5.2 Relationship Between Effective Pressure and Sliding Velocity

535 The three hydrology formulations do exhibit differences in $log(N_{eff})$ - $log(u_b)$ space. Linked-cavity hydrology exhibits a bimodal clustering at lower velocities/ higher effective pressures and higher velocities/lower effective pressures. This is a stark difference from the other two hydrologies. Further, the increased incidence of surge behaviour in the hydrology cases is not due to increased sliding – the no hydrology ensemble exhibits higher basal velocities than the three hydrology ensembles.

(a) LC

(c) PE

(b) LB

(d) NH
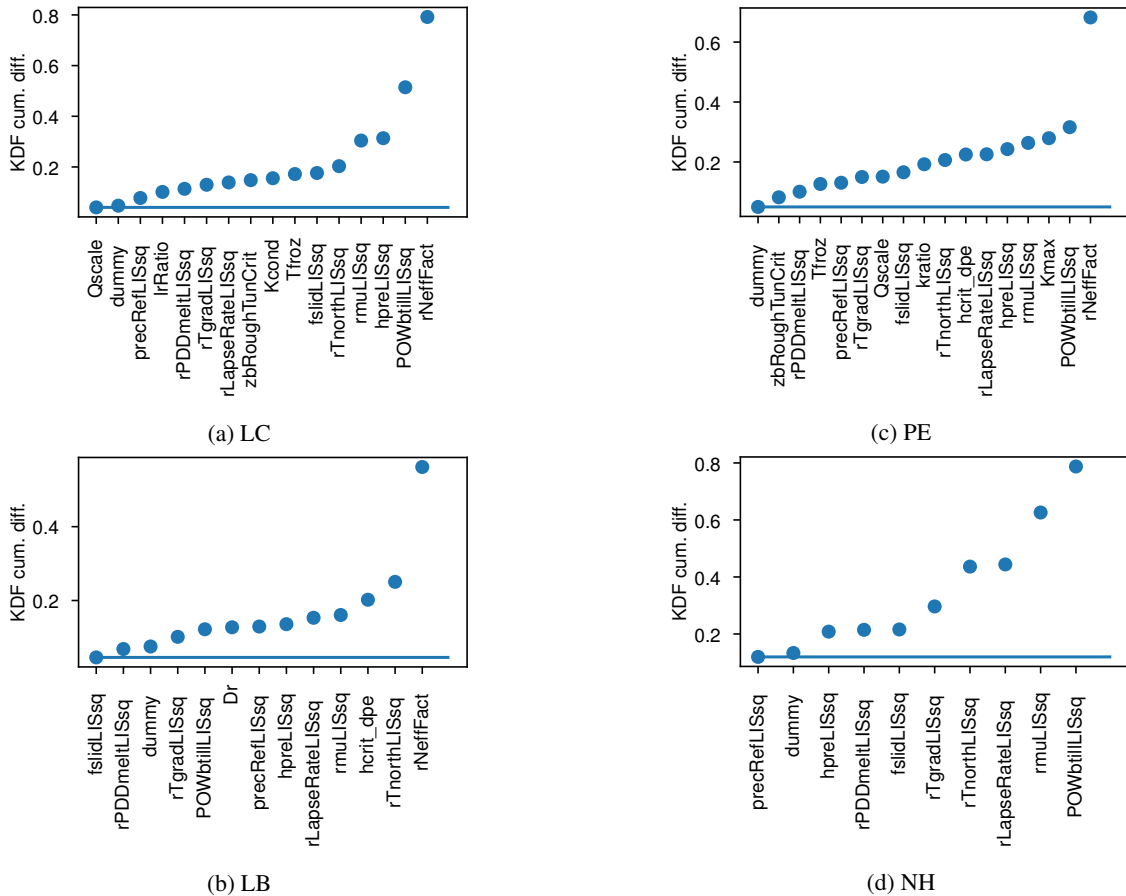
Figure 12. Parameters ranked by relative sensitivity for each model setup. Sensitivities measure the change in distribution from the geometry sieve to an additional surge frequency sieve, runs with 3 and more surges pass the surge frequency sieve.

6 Discussion of Surge Contribution

540 As we show above through sensitivity analysis and ensemble comparison of surge frequency and amplitude, subglacial hydrology is an important process that contributes to the feedbacks which govern Hudson Strait scale ice stream surging. While the process as a whole matters, the details matter less so – though it does depend on the aspects of ice stream surging under scrutiny. Across the three hydrology setups, the same range of HS basal velocity increase occurs: the magnitude of ice stream speed up is not dependent on the form of the subglacial hydrologic system and the three models can attain the same veloci-

545 ties within parametric uncertainty. This means that for model experiments looking to realistically capture ice stream surges, a leaky-bucket hydrology (the computationally cheapest of the three) is sufficient. Additionally, the range of frequency of HS surge occurrences is quite similar across the three hydrologies. However, the no hydrology case falls short of covering the range inferred for actual Heinrich Events attributed to HS surging (Naafs et al., 2013). This indicates that inclusion of some

| (a) LC | (b) PE | (c) LB | (d) NH |
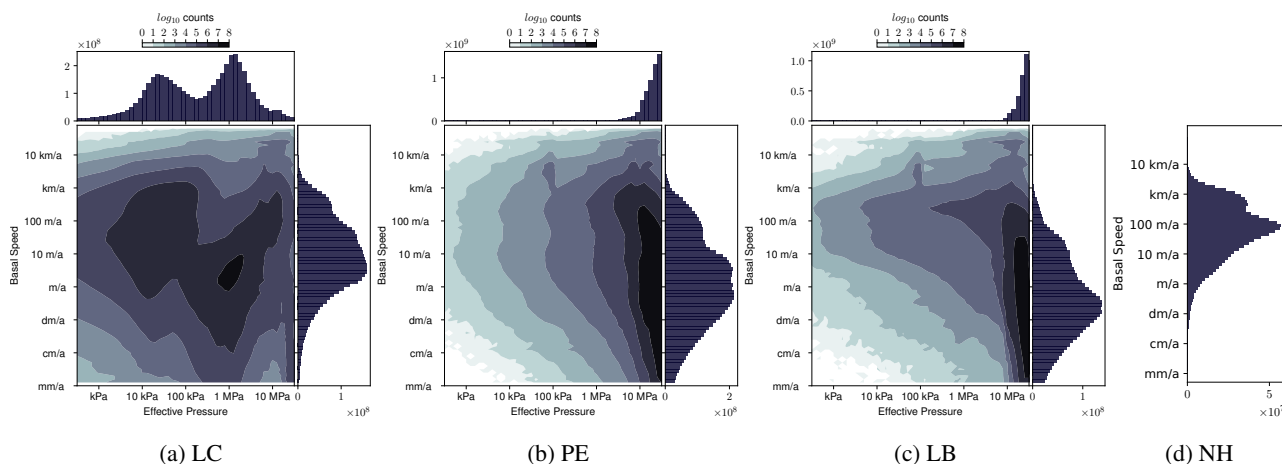
Figure 13. Two dimensional logarithmic histogram of effective pressure and velocity solutions for whole ensemble and all points in field where the subglacial hydrology system is active (that is, warm based). Fields are output every 100 years. Marginalized distribution for effective pressure and velocity shown along side, sharing the respective axes.

form of coupled subglacial hydrology is important for modelling large scale surge periodicities on geologic time scales. Once
550   again, however, the exact form of the subglacial hydrology does not matter for the periodicity of the surge onsets.

That the range of HS surge behaviour (frequency, amplitude) cannot be realistically captured absent subglacial hydrology is not due to a faster sliding coefficient. The effective pressure normalization is more than balanced by the effective pressure in the denominator in the basal velocity calculation. This is shown by the slower velocity distributions (min, mode, max) in the hydrology ensembles relative to the no hydrology configuration in fig. . The range of soft bed sliding coefficient covered in
555   each ensemble approaches the bounds of plausibility – rmu $\in [0.01, 4.0]$, where rmu is scaled to give a 3 km/a sliding velocity for 30 kPa basal drag. Increasing the sliding coefficient does not capture HS surge behaviour.

Increasing the lapse rate to non-physical bounds can increase the incidence of HS surge events in the no hydrology case. In the main experiments, the lapse rate is limited to the range $[5, 10]$ °C/km. However, increasing the lapse rates to $[10, 20]$ °C/km, increases the rate of surge events. This is because decreasing the surface temperature of ice in the Hudson Bay and Strait both
560   increases the vertical heat diffusion and decreases the temperature of ice advected to the base during a surge event. This enables a stronger thermomechanical surge termination mechanism.

Surge initiation at peak velocity for Hudson Strait scale ice streams as soon as the pressure melt point is reached is physically implausible. Basal velocity increases after ice becomes warm based and the effective pressure decreases. Inclusion of subglacial hydrology in the coupled system accomplishes this. The accommodation of increasing amounts of basal melt water
565   and pressurization (in the case that channelization does not occur) acts as a system inductance and the ice stream continues to speed up after becoming warm based. This inductance does not require the lateral transport of melt water – only the balance of melt water and a pressure closure dependence on subglacial water thickness.

Though periodicity and strength of surges are similar between the three hydrology bearing experiments, an interesting distinction occurs when examining the duration of events at varied frequencies. The stabilizing negative feedback of increasing effective pressure at higher basal velocities in the linked-cavity pressure closure gives surge durations longer (up to double, depending on frequency) than those of the diagnostic pressure closure of the poro-elastic and leaky-bucket hydrologies. This feedback also results in a bimodal effective pressure distribution (*i.e.*, fig. 6). When studying ice stream surge behaviour, any of the hydrologies may give the same surge response in terms of frequency and strength of surges. If the study requires a more granular understanding of how long the surge was active, for example when studying the surge timing of multiple ice streams in a catchment (*e.g.* Payne, 1998; Anandakrishnan and Alley, 1997) or the lifespan of palaeo-ice streams, our results suggest that accounting for the appropriate hydrology system is required.

7 Conclusions

The model presented herein passes multiple verification tests and as such is dependable for comparing the effects of structural choices of subglacial hydrology. The sensitivity analysis and ensemble comparison shows subglacial hydrology is an important control on both ice sheet geometry and on surging of major ice streams similar in scale to the Hudson Strait Ice Stream. However, depending on the characteristics of interest, the process details do not matter. The details do not matter for surge periodicity nor strength, but when studying the surge duration the hydrologic details are essential.

Surge behaviours can be produced in the absence of modelling a subglacial hydrology system but this requires unrealistic assumptions: pushing lapse rates to unrealistic ranges or implementing an un-physical sudden thaw in a large grid cell when the temperature reaches the pressure melt point. Subglacial hydrology provides a system inductance necessary for realistic ice speed up at the temperate transition. The critical components are the accommodation of melt water and a melt water pressure closure, not the mass conserving melt water transport itself.

Code and data availability. Data sets and code will be made available on publication

Appendix A: Surging With Thinner & Thicker Ice Sheets
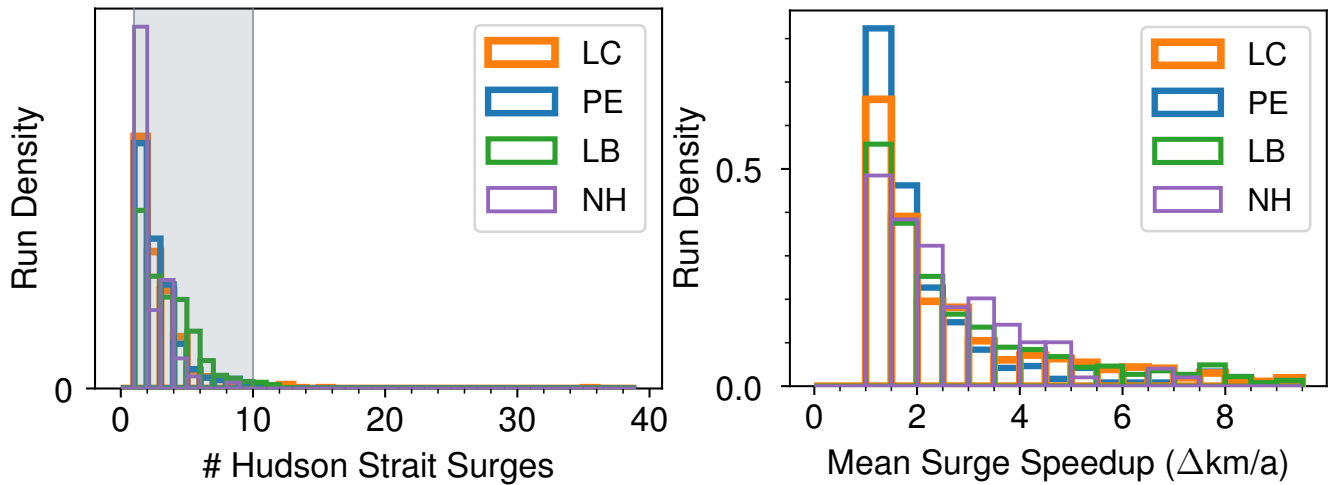
Figure A1. Histograms of Heinrich event metrics per parametrization for each model configuration for a thinner geometry sieve (2500 to 3500 m maximum ice thickness).
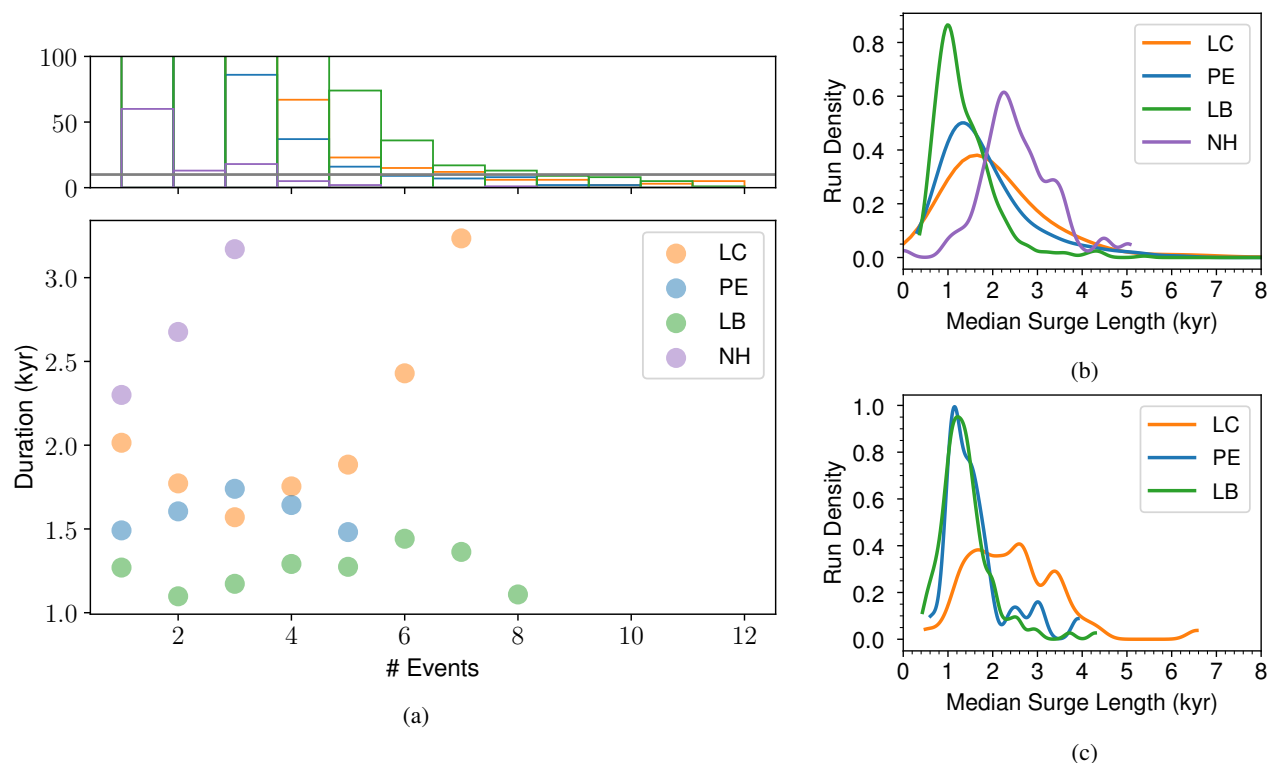
Figure A2. Surge event duration at different frequencies for thinner ice sheet sieve, $[2500, 3500]$ m. The scatterplot and histogram in (a) shows trends in median duration with increasing number of surges in a run. The overlying histogram shows the number of runs in each frequency sieve with the 10 run cutoff level shown by the horizontal grey line. The no-hydrology setup falls below this level after the three event bin, and the linked-cavity setup shows a divergence from the other two at this point. (b) and (c) show the kernel density functions of surge duration for runs with one to three and five to seven events respectively.
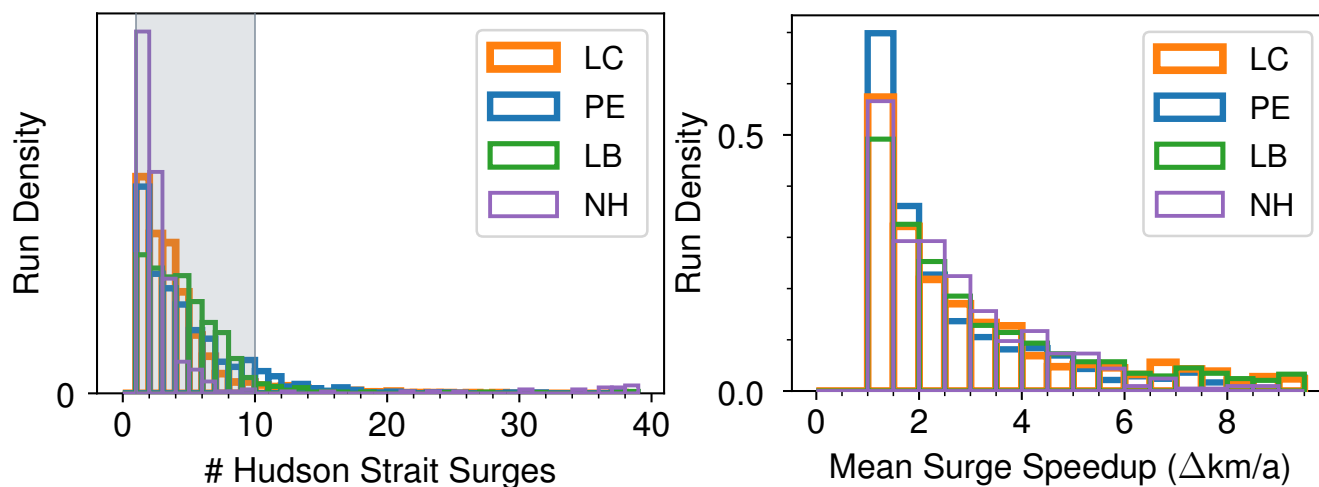
Figure A3. Sieve adjusted to $[3500, 4500]$ m. Histograms of Heinrich event metrics per parametrization for each model configuration.
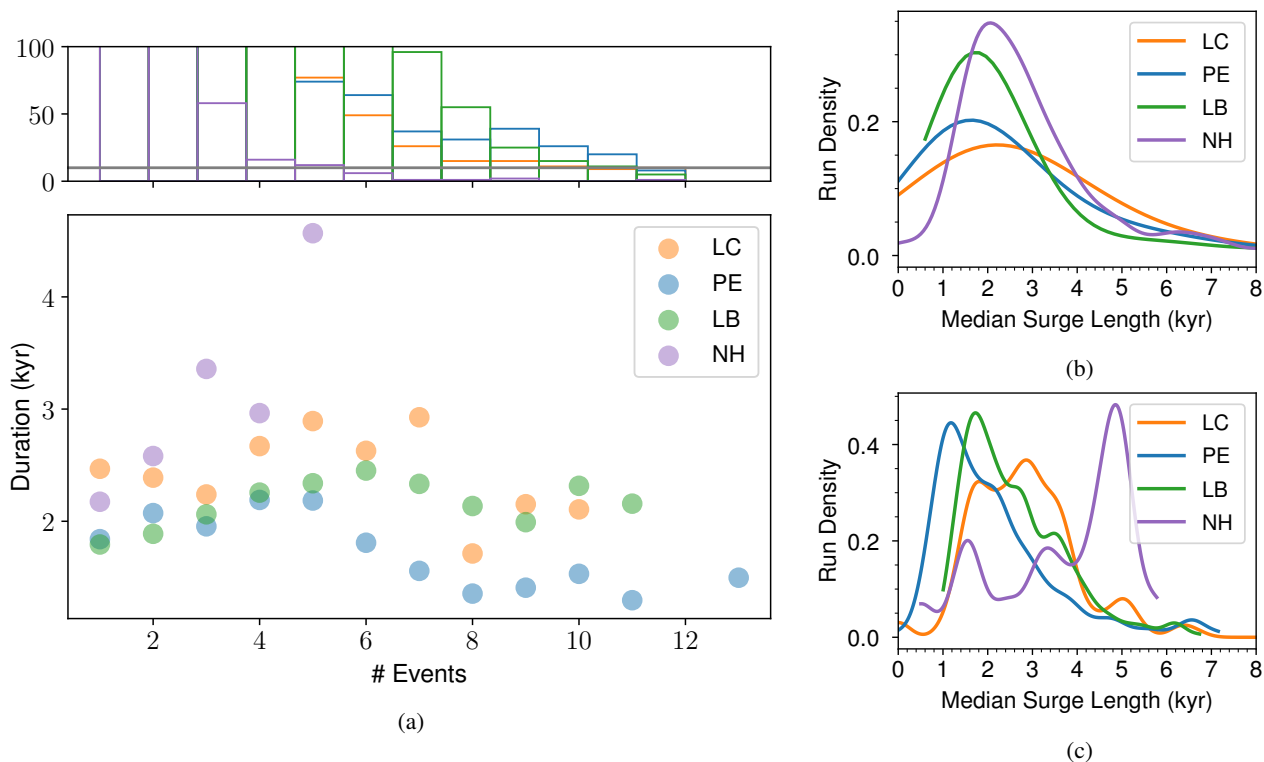
Figure A4. Surge event duration at different frequencies for thicker ice sheet sieve, $[3500, 4500]$ m. The scatterplot and histogram in (a) shows trends in median duration with increasing number of surges in a run. The overlying histogram shows the number of runs in each frequency sieve with the 10 run cutoff level shown by the horizontal grey line. The no-hydrology setup falls below this level after the three event bin, and the linked-cavity setup shows a divergence from the other two at this point. (b) and (c) show the kernel density functions of surge duration for runs with one to three and five to seven events respectively.

590 **Appendix B: Verification**
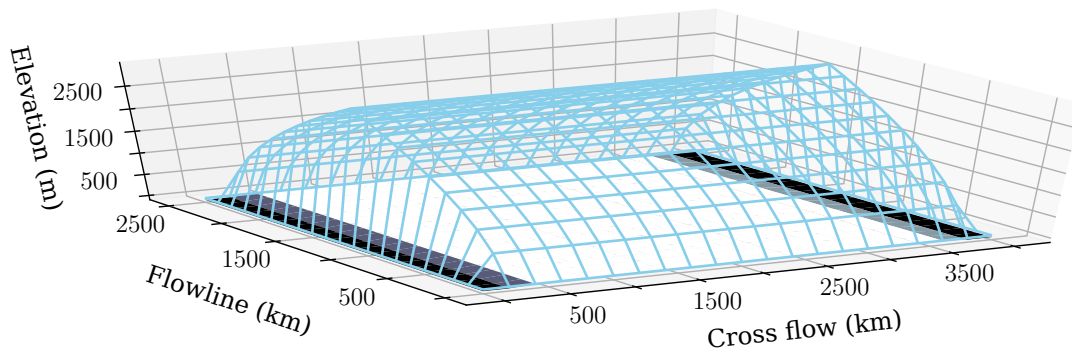
Figure B1. Ice sheet configuration used in SHMIP with basal temperature (black=-40,white=0.01)

The $net_{hyd}^{t_i}$ time series was then compared against modelled total water volume ($V_{hyd}^{t_i}$) to calculate mass conservation error (ERR^{t_i}):

$$ERR_{hyd}^{t_i} = \frac{|net_{hyd}^{t_i} - V_{hyd}^{t_i}|}{V_{hyd}^{t_i}} \qquad \text{(B1)}$$

net_{hyd} is given in eqn. 17 and V_{hyd} is the volume of water under the ice sheet.
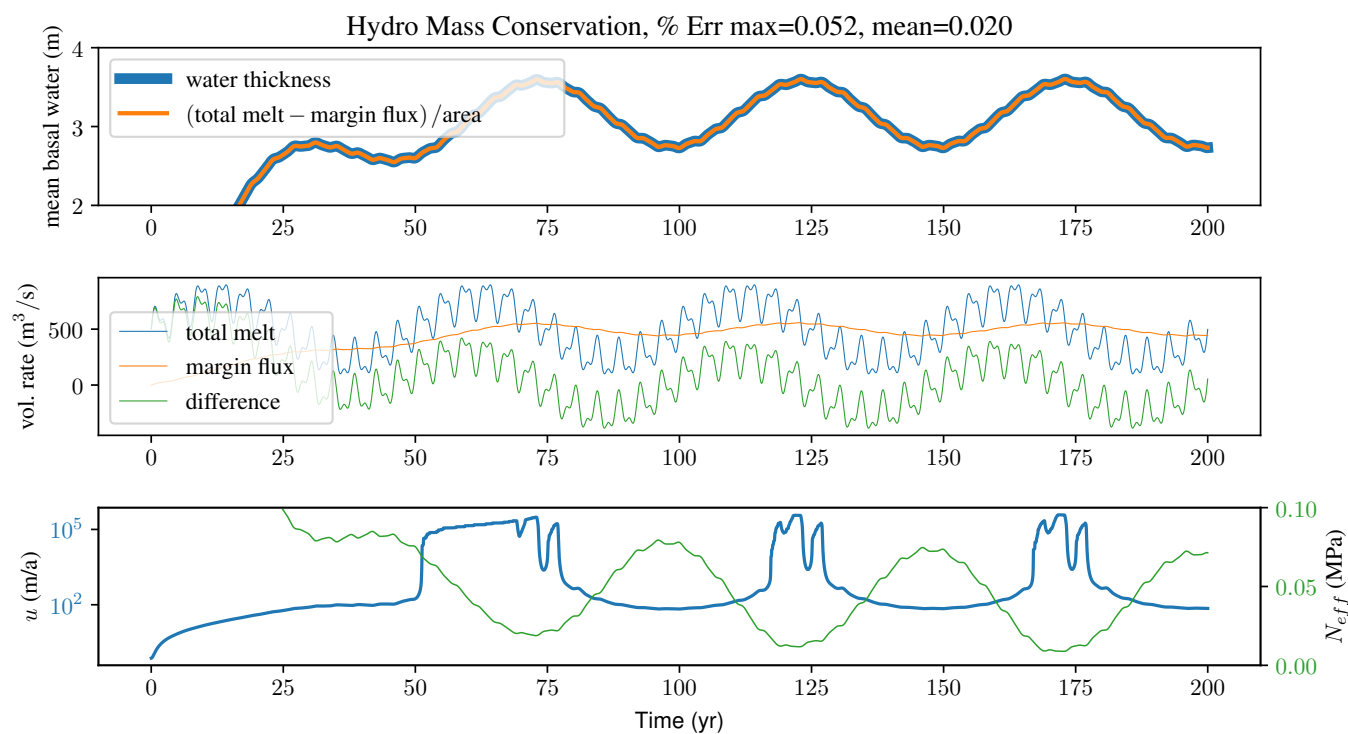
Figure B2. Assessment of mass conservation for subglacial hydrology model given steady square root ice sheet topography, flat basal topography, and sinusoidal ice sheet basal melt water generation (m/a) given in eqn. 12, The basal sliding velocity calculated from driving stress and effective pressure (eqn. 14) over a 200 year modelled time period. The model solution for basal water thickness is compared with the time integrated difference of basal melt and flux out of the margin (eqn. 17) in the top panel (near complete visual overlap). For an illustration of model input and response, the centre panel shows the basal melt water, flux out of the margin and the difference between the two over time. The bottom panel shows dynamically calculated, two way coupled basal velocity in blue and effective pressure in green.

Appendix C: Subglacial Hydrology Model Assumptions

595

The physics of the linked cavity system is highly non-linear. As such, a set of simplifying assumptions is required to make numerical modelling of this framework feasible:

1. Wall melting is not a control on cavity size until tunnels are opened. Drainage systems switch from inefficient to efficient for a given value of flux. Schoof (2010) showed the evolution of the subglacial drainage system (described in eqn. 7)

600 gives a bifurcation between cavity style and tunnel style drainage networks. Given effective pressure, the cavity opening speed is dominated by basal sliding below a certain flux and by run away wall melting above it.

2. At time scales of continental scale ice sheets, tunnels drain water instantaneously. The time scale of drainage through subglacial tunnels is less than a single melt season, much shorter than the centennial to millennial scale changes this model is applied to. This assumption alleviates CFL violations from fast tunnel flux which would render modelling on

605 the long time scales of glacial cycles infeasible.

3. Cavities are filled with water. Consider the time scale for closure of a recently drained cavity given various combinations of ice sheet overburden (thickness, m) and sliding velocities. This time scale for closure (from eqn. 8) is given by:

$$T = \frac{S}{u_b h_r - c_2 N^3 S} \tag{C1}$$

The range of time scales, assuming speed in range 1-1000 m/a and ice overburden thickness greater than 200 m is shown

610 in fig. C1 where the maximum time for closure is around two weeks, less than the minimum time step of 0.125 yr in the hydrology model.
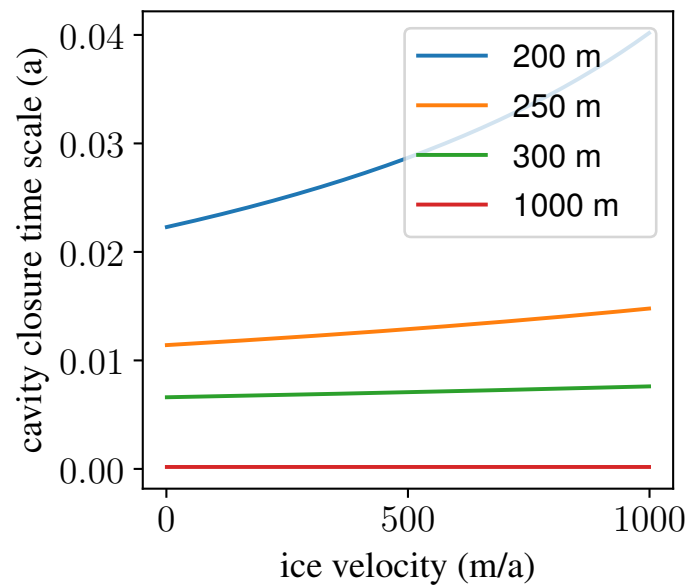
Figure C1. Cavity closure times at varied ice sheet thickness and sliding speeds.

Appendix D: Discretization

D1 Pressure Closure of Bueler and van Pelt (2015)

Here we use the time varying water pressure calculation of Bueler and van Pelt (2015). The rationale summarized here is
shown by Bueler (2014). Here the subglacial and englacial hydrologic systems are assumed in perfect communication and
their co-evolution is described. The englacial hydrologic system is analogized to a rigid "pore-space" (comprised of crevasses,
moulins, englacial channels, and inter-granular porosity). The **tot**al volume of water is the sum of **eng**lacial and **sub**glacial
water:

$$V_{tot} = V_{eng} + V_{sub} \tag{D1}$$

and the mass balance for incompressible water is

$$\frac{\partial V_{tot}}{\partial t} = -Q_{out} + Q_{in} + \frac{m}{\rho_w} \tag{D2}$$

from total flux in and out of a control section of the system plus any sources (volume water, $\frac{m}{\rho_w}$) within that section. This
section is of area Δx by Δy and pressure in the connected englacial-subglacial system is given by the hydrostatic head in the
englacial part:

$$P_w = \frac{\rho_w g}{\Delta x \Delta y \phi_{eng}} V_{eng}. \tag{D3}$$

The effective englacial porosity (ice volume relative proportion of connected englacial void space) is ϕ_{eng}. Cavity volume
within an area of bed with roughness wavelength l_r (cavity generating obstacle spacing) is:

$$V_{sub} = n_{cav} V_{cav} = \frac{\Delta x \Delta y}{l_r{}^2} V_{cav} \tag{D4}$$

where n_{cav} is the number of cavities in the given bed section and V_{cav} is their average volume. Differentiating this gives the
change in pressure with time:

$$\begin{aligned}
\frac{\partial P_w}{\partial t} &= \frac{\rho_w g}{\Delta x \Delta y \phi_{eng}} \frac{\partial V_{eng}}{\partial t} \\
&= \frac{\rho_w g}{\Delta x \Delta y \phi_{eng}} \frac{\partial V_{tot} - V_{sub}}{\partial t} \\
&= \frac{\rho_w g}{\Delta x \Delta y \phi_{eng}} \left\{ Q_{in} - Q_{out} + \frac{m}{\rho_w} - \frac{\Delta x \Delta y}{l_r{}^2} \frac{\partial V_{cav}}{\partial t} \right\}
\end{aligned}$$

The $\left(1/l_r^2 \right) \frac{\partial V_{cav}}{\partial t} = \frac{\partial h_{cav}}{\partial t}$ derivative is given by the opening and closing balance in eqn. **??**,

$$\frac{\partial P_w}{\partial t} = \frac{\rho_w g}{\phi_{eng}} \left\{ \frac{Q_{in} - Q_{out} + \frac{m}{\rho_w}}{\Delta x \Delta y} - u_b \left(h_r - h_{wb} \right) / l_r + c_2 [P_{ice} - P_w]^n \right\}. $$

Here opening due to wall melting has been omitted (see Assumption 1) relative to what is shown by Bueler (2014). As $\Delta x \to 0$
and $\Delta y \to 0$ the difference of the fluxes in versus out of the control section goes to the divergence of the fluxes within it.

$$\frac{\partial P_w}{\partial t} = \frac{\rho_w g}{\phi_{eng}} \left\{ -\nabla \cdot \mathbf{Q} + m_t - u_b \left(h_r - h_{wb} \right) / l_r - c_2 [P_{ice} - P_w]^n \right\}. \tag{D5}$$

with m_t the source of water in thickness per unit time. we assume that water only travels laterally through the subglacial system
640 and so all fluxes are through the linked cavities.

Author contributions. MD performed subglacial hydrology model development, experimental design & execution, analysis, and writing. LT
maintains the GSM, advised experimental design, and manuscript editing

Competing interests. The authors declare no competing interests

Acknowledgements. Figures generated with matplotlib (Hunter, 2007).

References

Alley, R.: Water-Pressure Coupling of Sliding and Bed Deformation: I. Water System, Journal of Glaciology, 35, 108–118, https://doi.org/10.3189/002214389793701527, 1989.

Alley, R. B.: How can low-pressure channels and deforming tills coexist subglacially?, Journal of Glaciology, 38, 200–207, https://doi.org/10.3189/s0022143000009734, 1992.

Alley, R. B., Anandakrishnan, S., Bentley, C. R., and Lord, N.: A water-piracy hypothesis for the stagnation of Ice Stream C, Antarctica, Annals of Glaciology, 20, 187–194, https://doi.org/10.3189/1994aog20-1-187-194, 1994.

Anandakrishnan, S. and Alley, R. B.: Stagnation of Ice Stream C, West Antarctica by water piracy, Geophysical Research Letters, 24, 265–268, https://doi.org/10.1029/96gl04016, 1997.

Anderson, R. S., Hallet, B., Walder, J., and Aubry, B. F.: Observations in a cavity beneath grinnell glacier, Earth Surface Processes and Landforms, 7, 63–70, https://doi.org/10.1002/esp.3290070108, 1982.

Bennett, M. R.: Ice streams as the arteries of an ice sheet: their mechanics, stability and significance, Earth-Science Reviews, 61, 309–339, https://doi.org/10.1016/s0012-8252(02)00130-7, 2003.

Brubaker, K. M., Myers, W. L., Drohan, P. J., Miller, D. A., and Boyer, E. W.: The Use of LiDAR Terrain Data in Characterizing Surface Roughness and Microtopography, Applied and Environmental Soil Science, 2013, 1–13, https://doi.org/10.1155/2013/891534, 2013.

Bueler, E.: Extending the lumped subglacial–englacial hydrology model of Bartholomaus and others (2011), Journal of Glaciology, 60, 808–810, https://doi.org/10.3189/2014jog14j075, 2014.

Bueler, E. and van Pelt, W.: Mass-conserving subglacial hydrology in the Parallel Ice Sheet Model version 0.6, Geoscientific Model Development, 8, 1613–1635, https://doi.org/10.5194/gmd-8-1613-2015, 2015.

Calov, R., Greve, R., Abe-Ouchi, A., Bueler, E., Huybrechts, P., Johnson, J. V., Pattyn, F., Pollard, D., Ritz, C., Saito, F., and et al.: Results from the Ice-Sheet Model Intercomparison Project–Heinrich Event Intercomparison (ISMIP HEINO), Journal of Glaciology, 56, 371–383, https://doi.org/10.3189/002214310792447789, 2010.

Carsey, F., Behar, A., Lonne Lane, A., Realmuto, V., and Engelhardt, H.: A borehole camera system for imaging the deep interior of ice sheets, Journal of Glaciology, 48, 622–628, https://doi.org/10.3189/172756502781831124, 2002.

Chandler, D. M., Wadham, J. L., Lis, G. P., Cowton, T., Sole, A., Bartholomew, I., Telling, J., Nienow, P., Bagshaw, E. B., Mair, D., and et al.: Evolution of the subglacial drainage system beneath the Greenland Ice Sheet revealed by tracers, Nature Geoscience, 6, 195–198, https://doi.org/10.1038/ngeo1737, 2013.

Clark, P. U., Archer, D., Pollard, D., Blum, J. D., Rial, J. A., Brovkin, V., Mix, A. C., Pisias, N. G., and Roy, M.: The middle Pleistocene transition: characteristics, mechanisms, and implications for long-term changes in atmospheric pCO2, Quaternary Science Reviews, 25, 3150–3184, https://doi.org/10.1016/j.quascirev.2006.07.008, 2006.

Clarke, G. K. C.: Lumped-element analysis of subglacial hydraulic circuits, Journal of Geophysical Research: Solid Earth, 101, 17 547–17 559, https://doi.org/10.1029/96jb01508, 1996.

Courant, R., Friedrichs, K., and Lewy, H.: Über die partiellen Differenzengleichungen der mathematischen Physik, Mathematische Annalen, 100, 32–74, https://doi.org/10.1007/bf01448839, 1928.

Dalton, A. S., Margold, M., Stokes, C. R., Tarasov, L., Dyke, A. S., Adams, R. S., Allard, S., Arends, H. E., Atkinson, N., Attig, J. W., Barnett, P. J., Barnett, R. L., Batterson, M., Bernatchez, P., Borns, H. W., Breckenridge, A., Briner, J. P., Brouard, E., Campbell, J. E., Carlson, A. E., Clague, J. J., Curry, B. B., Daigneault, R.-A., Dubé-Loubert, H., Easterbrook, D. J., Franzi, D. A., Friedrich, H. G., Funder,

S., Gauthier, M. S., Gowan, A. S., Harris, K. L., Hétu, B., Hooyer, T. S., Jennings, C. E., Johnson, M. D., Kehew, A. E., Kelley, S. E.,
Kerr, D., King, E. L., Kjeldsen, K. K., Knaeble, A. R., Lajeunesse, P., Lakeman, T. R., Lamothe, M., Larson, P., Lavoie, M., Loope, H. M.,
Lowell, T. V., Lusardi, B. A., Manz, L., McMartin, I., Nixon, F. C., Occhietti, S., Parkhill, M. A., Piper, D. J., Pronk, A. G., Richard, P. J.,
Ridge, J. C., Ross, M., Roy, M., Seaman, A., Shaw, J., Stea, R. R., Teller, J. T., Thompson, W. B., Thorleifson, L. H., Utting, D. J., Veillette,
J. J., Ward, B. C., Weddle, T. K., and Wright, H. E.: An updated radiocarbon-based ice margin chronology for the last deglaciation of the
North American Ice Sheet Complex, Quaternary Science Reviews, 234, 106 223, https://doi.org/10.1016/j.quascirev.2020.106223, 2020.

Darcy, H.: Les Fontaines Publiques De La Ville De Dijon: Exposition Et Application Des Principes A Suivre Et Des Formules A Employer
Dans Les Questions De Distribution D'eau, Librairie des corps impériaux des ponts et chaussées et des mines, 49 Quai des Augustins,
Paris, France, 1 edn., 1856.

de Fleurian, B., Werder, M. A., Beyer, S., Brinkerhoff, D. J., Delaney, I., Dow, C. F., Downs, J., Gagliardini, O., Hoffman, M. J., Hooke,
R. L., Seguinot, J., and Sommers, A. N.: SHMIP The subglacial hydrology model intercomparison Project, Journal of Glaciology, 64,
897–916, https://doi.org/10.1017/jog.2018.78, 2018.

Dowdeswell, J. A., Maslin, M. A., Andrews, J. T., and McCave, I. N.: Iceberg production, debris rafting, and the extent and thickness of Hein-
rich layers (H-1, H-2) in North Atlantic sediments, Geology, 23, 301, https://doi.org/10.1130/0091-7613(1995)023<0297:ipdrat>2.3.co;2,
1995.

Erokhina, O., Rogozhina, I., Prange, M., Bakker, P., Bernales, J., Paul, A., and Schulz, M.: Dependence of slope lapse rate over the Greenland
ice sheet on background climate, Journal of Glaciology, 63, 568–572, https://doi.org/10.1017/jog.2017.10, 2017.

Flowers, G. E.: A Multicomponent Coupled Model of Glacier Hydrology, Ph.D. thesis, University of British Columbia, Department of Earth,
Ocean and Atmospheric Sciences Faculty of Science 2020 – 2207 Main Mall Vancouver, BC Canada V6T 1Z4, 2000.

Flowers, G. E.: Modelling water flow under glaciers and ice sheets, Proceedings of the Royal Society A: Mathematical, Physical and Engi-
neering Sciences, 471, 1–41, https://doi.org/10.1098/rspa.2014.0907, 2015.

Flowers, G. E.: Hydrology and the future of the Greenland Ice Sheet, Nature Communications, 9, https://doi.org/10.1038/s41467-018-05002-
0, 2018.

Flowers, G. E. and Clarke, G. K. C.: A multicomponent coupled model of glacier hydrology 1. Theory and synthetic examples, Journal of
Geophysical Research: Solid Earth, 107, ECV 9–1–ECV 9–17, https://doi.org/10.1029/2001jb001122, 2002.

Fowler, A. C.: Instability modelling of drumlin formation incorporating lee-side cavity growth, Proceedings of the Royal Society A: Mathe-
matical, Physical and Engineering Sciences, 465, 2681–2702, https://doi.org/10.1098/rspa.2008.0490, 2009.

Fricker, H. A., Siegfried, M. R., Carter, S. P., and Scambos, T. A.: A decade of progress in observing and modelling Antarctic subglacial
water systems, Philosophical Transactions of the Royal Society A: Mathematical, Physical and Engineering Sciences, 374, 20140 294,
https://doi.org/10.1098/rsta.2014.0294, 2016.

Gandy, N., Gregoire, L. J., Ely, J. C., Cornford, S. L., Clark, C. D., and Hodgson, D. M.: Exploring the ingredients required to successfully
model the placement, generation, and evolution of ice streams in the British-Irish Ice Sheet, Quaternary Science Reviews, 223, 105 915,
https://doi.org/10.1016/j.quascirev.2019.105915, 2019.

Grinsted, A., Hvidberg, C. S., Lilien, D. A., Rathmann, N. M., Karlsson, N. B., Gerber, T., Kjær, H. A., Vallelonga, P., and Dahl-Jensen, D.:
Accelerating ice flow at the onset of the Northeast Greenland Ice Stream, Nature Communications, 13, https://doi.org/10.1038/s41467-
022-32999-2, 2022.

Hemming, S. R.: Heinrich events: Massive late Pleistocene detritus layers of the North Atlantic and their global climate imprint, Reviews of
Geophysics, 42, https://doi.org/10.1029/2003rg000128, 2004.

720   Herman, J. and Usher, W.: SALib: An open-source Python library for Sensitivity Analysis, The Journal of Open Source Software, 2, 97, https://doi.org/10.21105/joss.00097, 2017.

Hewitt, I.: Seasonal changes in ice sheet motion due to melt water lubrication, Earth and Planetary Science Letters, 371-372, 16–25, https://doi.org/10.1016/j.epsl.2013.04.022, 2013.

Hunter, J. D.: Matplotlib: A 2D graphics environment, Computing in Science & Engineering, 9, 90–95,
725   https://doi.org/10.1109/MCSE.2007.55, 2007.

Iverson, N. R.: A theory of glacial quarrying for landscape evolution models, Geology, 40, 679–682, https://doi.org/10.1130/g33079.1, 2012.

Joughin, I., Tulaczyk, S., Fahnestock, M., and Kwok, R.: A Mini-Surge on the Ryder Glacier, Greenland, Observed by Satellite Radar Interferometry, Science, 274, 228–230, https://doi.org/10.1126/science.274.5285.228, 1996.

Kageyama, M., Harrison, S. P., Kapsch, M.-L., Lofverstrom, M., Lora, J. M., Mikolajewicz, U., Sherriff-Tadano, S., Vadsaria, T., Abe-
730   Ouchi, A., Bouttes, N., and et al.: The PMIP4 Last Glacial Maximum experiments: preliminary results and comparison with the PMIP3 simulations, Climate of the Past, 17, 1065–1089, https://doi.org/10.5194/cp-17-1065-2021, 2021.

Kamb, B.: Glacier surge mechanism based on linked cavity configuration of the basal water conduit system, Journal of Geophysical Research, 92, 9083–9100, https://doi.org/10.1029/jb092ib09p09083, 1987.

Kavanagh, M. and Tarasov, L.: BrAHMs V1.0: a fast, physically based subglacial hydrology model for continental-scale application, Geo-
735   scientific Model Development, 11, 3497–3513, https://doi.org/10.5194/gmd-11-3497-2018, 2018.

Kingslake, J. and Ng, F.: Modelling the coupling of flood discharge with glacier flow during jökulhlaups, Annals of Glaciology, 54, 25–31, https://doi.org/10.3189/2013aog63a331, 2013.

Lawrence, M. G.: The Relationship between Relative Humidity and the Dewpoint Temperature in Moist Air: A Simple Conversion and Applications, Bulletin of the American Meteorological Society, 86, 225–234, https://doi.org/10.1175/bams-86-2-225, 2005.

740   MacAyeal, D. R.: Binge/purge oscillations of the Laurentide Ice Sheet as a cause of the North Atlantic's Heinrich events, Paleoceanography, 8, 775–784, https://doi.org/10.1029/93pa02200, 1993.

Mathews, W. H.: Surface profiles of the laurentide ice sheet in its marginal areas, Journal of Glaciology, 13, 37–43, https://doi.org/10.1017/s0022143000023352, 1974.

Morlighem, M., Rignot, E., Mouginot, J., Wu, X., Seroussi, H., Larour, E., and Paden, J.: High-resolution bed topogra-
745   phy mapping of Russell Glacier, Greenland, inferred from Operation IceBridge data, Journal of Glaciology, 59, 1015–1023, https://doi.org/10.3189/2013jog12j235, 2013.

Muskat, M.: The Flow of Compressible Fluids Through Porous Media and Some Problems in Heat Conduction, Physics, 5, 71–94, https://doi.org/10.1063/1.1745233, 1934.

Naafs, B., Hefter, J., and Stein, R.: Millennial-scale ice rafting events and Hudson Strait Heinrich(-like) Events during the late Pliocene and
750   Pleistocene: a review, Quaternary Science Reviews, 80, 1–28, https://doi.org/10.1016/j.quascirev.2013.08.014, 2013.

Oreskes, N., Shrader-Frechette, K., and Belitz, K.: Verification, Validation, and Confirmation of Numerical Models in the Earth Sciences, Science, 263, 641–646, https://doi.org/10.1126/science.263.5147.641, 1994.

Ou, H.-W.: A theory of glacier dynamics and instabilities Part 1: Topographically confined glaciers, Journal of Glaciology, p. 1–12, https://doi.org/10.1017/jog.2021.20, 2021.

755   Patankar, S. V.: Numerical Heat Transfer and Fluid Flow, McGraw-Hill Book Company, 1221 Avenue of the Americas, New York, New York, USA, 1 edn., 1980.

Payne, A. J.: Dynamics of the Siple Coast ice streams, west Antarctica: Results from a thermomechanical ice sheet model, Geophysical Research Letters, 25, 3173–3176, https://doi.org/10.1029/98gl52327, 1998.

Payne, A. J. and Dongelmans, P. W.: Self-organization in the thermomechanical flow of ice sheets, Journal of Geophysical Research: Solid Earth, 102, 12 219–12 233, https://doi.org/10.1029/97jb00513, 1997.

Payne, A. J., Huybrechts, P., Abe-Ouchi, A., Calov, R., Fastook, J. L., Greve, R., Marshall, S. J., Marsiat, I., Ritz, C., Tarasov, L., and et al.: Results from the EISMINT model intercomparison: the effects of thermomechanical coupling, Journal of Glaciology, 46, 227–238, https://doi.org/10.3189/172756500781832891, 2000.

Pelletier, J. D., Broxton, P. D., Hazenberg, P., Zeng, X., Troch, P. A., Niu, G.-Y., Williams, Z., Brunke, M. A., and Gochis, D.: A gridded global data set of soil, intact regolith, and sedimentary deposit thicknesses for regional and global land surface modeling, Journal of Advances in Modeling Earth Systems, 8, 41–65, https://doi.org/10.1002/2015ms000526, 2016.

Pollard, D. and DeConto, R. M.: A simple inverse method for the distribution of basal sliding coefficients under ice sheets, applied to Antarctica, The Cryosphere, 6, 953–971, https://doi.org/10.5194/tc-6-953-2012, 2012.

Retzlaff, R. and Bentley, C. R.: Timing of stagnation of Ice Stream C, West Antarctica, from short-pulse radar studies of buried surface crevasses, Journal of Glaciology, 39, 553–561, https://doi.org/10.3189/s0022143000016440, 1993.

Roache, P. J.: QUANTIFICATION OF UNCERTAINTY IN COMPUTATIONAL FLUID DYNAMICS, Annual Review of Fluid Mechanics, 29, 123–160, https://doi.org/10.1146/annurev.fluid.29.1.123, 1997.

Röthlisberger, H.: Water Pressure in Intra- and Subglacial Channels, Journal of Glaciology, 11, 177–203, https://doi.org/10.3189/s0022143000022188, 1972.

Saltelli, A.: Making best use of model evaluations to compute sensitivity indices, Computer Physics Communications, 145, 280–297, https://doi.org/10.1016/s0010-4655(02)00280-1, 2002.

Saltelli, A., Ratto, M., Andres, T., Campolongo, F., Cariboni, J., Gatelli, D., Saisana, M., and Tarantola, S.: Global Sensitivity Analysis, John Wiley & Sons, Ltd., The Atrium, Southern Gate, Chichester,West Sussex PO19 8SQ, England, 1 edn., 2008.

Schoof, C.: Cavitation on Deformable Glacier Beds, SIAM Journal on Applied Mathematics, 67, 1633–1653, https://doi.org/10.1137/050646470, 2007.

Schoof, C.: Ice-sheet acceleration driven by melt supply variability, Nature, 468, 803–806, https://doi.org/10.1038/nature09618, 2010.

Siegfried, M. R., Fricker, H. A., Carter, S. P., and Tulaczyk, S.: Episodic ice velocity fluctuations triggered by a subglacial flood in West Antarctica, Geophysical Research Letters, 43, 2640–2648, https://doi.org/10.1002/2016gl067758, 2016.

Sobol, I.: Global sensitivity indices for nonlinear mathematical models and their Monte Carlo estimates, Mathematics and Computers in Simulation, 55, 271–280, https://doi.org/10.1016/s0378-4754(00)00270-6, 2001.

Sornette, D., Davis, A. B., Ide, K., Vixie, K. R., Pisarenko, V., and Kamm, J. R.: Algorithm for model validation: Theory and applications, Proceedings of the National Academy of Sciences, 104, 6562–6567, https://doi.org/10.1073/pnas.0611677104, 2007.

Tarasov, L. and Peltier, W.: A calibrated deglacial drainage chronology for the North American continent: evidence of an Arctic trigger for the Younger Dryas, Quaternary Science Reviews, 25, 659–688, https://doi.org/10.1016/j.quascirev.2005.12.006, 2006.

Tarasov, L. and Peltier, W. R.: Coevolution of continental ice cover and permafrost extent over the last glacial-interglacial cycle in North America, Journal of Geophysical Research, 112, https://doi.org/10.1029/2006jf000661, 2007.

Tarasov, L., Dyke, A. S., Neal, R. M., and Peltier, W. R.: A Data-Calibrated Distribution of Deglacial Chronologies for the North American Ice Complex from Glaciological Modeling, Earth and Planetary Science Letters, pp. 30–40, 2012.

Virtanen, P., Gommers, R., Oliphant, T. E., Haberland, M., Reddy, T., Cournapeau, D., Burovski, E., Peterson, P., Weckesser, W., Bright, J.,
795   van der Walt, S. J., Brett, M., Wilson, J., Millman, K. J., Mayorov, N., Nelson, A. R. J., Jones, E., Kern, R., Larson, E., Carey, C. J., Polat,
       İ., Feng, Y., Moore, E. W., VanderPlas, J., Laxalde, D., Perktold, J., Cimrman, R., Henriksen, I., Quintero, E. A., Harris, C. R., Archibald,
       A. M., Ribeiro, A. H., Pedregosa, F., van Mulbregt, P., and SciPy 1.0 Contributors: SciPy 1.0: Fundamental Algorithms for Scientific
       Computing in Python, Nature Methods, 17, 261–272, https://doi.org/10.1038/s41592-019-0686-2, 2020.

Walder, J. and Hallet, B.: Geometry of Former Subglacial Water Channels and Cavities, Journal of Glaciology, 23, 335–346,
800   https://doi.org/10.1017/s0022143000029944, 1979.

Walder, J. S.: Hydraulics of Subglacial Cavities, Journal of Glaciology, 32, 439–445, https://doi.org/10.3189/s0022143000012156, 1986.

Walder, J. S. and Fowler, A.: Channelized subglacial drainage over a deformable bed, Journal of Glaciology, 40, 3–15,
       https://doi.org/10.3189/s0022143000003750, 1994.

Weisbach, J.: Lehrbuch der ingenieur- und maschinen-mechanik, Vieweg, Braunschweig, Germany, 1 edn., https://babel.hathitrust.org/cgi/
805   pt?id=wu.89088908009&view=1up&seq=8, 1855.

Werder, M. A., Hewitt, I. J., Schoof, C. G., and Flowers, G. E.: Modeling channelized and distributed subglacial drainage in two dimensions,
       Journal of Geophysical Research: Earth Surface, 118, 2140–2158, https://doi.org/10.1002/jgrf.20146, 2013.

Willis, M. J., Zheng, W., Durkin, W. J., Pritchard, M. E., Ramage, J. M., Dowdeswell, J. A., Benham, T. J., Bassford, R. P., Stearns, L. A.,
       Glazovsky, A. F., Macheret, Y. Y., and Porter, C. C.: Massive destabilization of an Arctic ice cap, Earth and Planetary Science Letters,
810   502, 146–155, https://doi.org/10.1016/j.epsl.2018.08.049, 2018.